Selective Laser Melting of Finemet Soft Magnetic Material

Haozheng Wang

Thesis submitted to faculty of the Virginia Polytechnic Institute and State University in partial fulfillment of the requirements for the degree of

Master of Science

In

Material Science and Engineering

Hang Yu, Chair Advisor

Lei Zuo, Co-Advisor

William Reynolds

Wenjun Cai

Aug 25th, 2023

Blacksburg, VA

Keywords: Selective Laser Melting, Processing Parameters Optimization, Finemet Soft Magnetic Materials, L-PBF Additive Manufacturing, Functional Property Characterization, Microstructural Feature, Solute Segregation

Selective Laser Melting of Finemet Soft Magnetic Material

Haozheng Wang

ABSTRACT

Soft magnetic materials have been widely used in electric motors, routers, and detectors. Tremendous studies have been conducted to report microstructural features corresponding to magnetic performance. The laser-based powder bed fusion (L-PBF) additive manufacturing technique was implemented to bulk-scale fabricate the Finemet nanocrystalline magnetic alloy. This research study aims to reveal the capability of replacing the traditional melt spinning process with decent bulk density and magnetic properties. Nanocrystalline materials originate from optimizing amorphous metallic alloys, resulting in low coercivity and high saturation magnetization by facilitating the formation of nanocrystals. An extremely high cooling rate is the foundational factor for controlling the microstructure. Selective Laser Melting (SLM) offers a layer thickness of 20-100 μm, naturally providing a cooling rate of 10^5 - 10^7 K/s. Subsequent melting will impact the microstructure by conducting heat continuously through the melt pools. The relationship between microstructural features and crystalline phase characterization is discussed. Magnetic characterization, in terms of saturation magnetization and coercivity, with various processing parameters, is investigated.

Selective Laser Melting of Finemet Soft Magnetic Material

Haozheng Wang

GENERAL AUDIENCE ABSTRACT

Magnetic materials are used in everyday devices like electric motors and routers. They're made in special ways to have specific structures which give them their magnetic properties. One of the latest techniques we've explored to make these materials is using lasers to melt and fuse powder, much like how 3D printer’s work. Our study focused on creating a special kind of magnetic material called "Finemet." We wanted to see if this laser method could be an alternative to the usual way, we bulk scale synthesis this material. In simple terms, the Finemet material is made by tweaking certain metallic mixes to have tiny crystals that improve its magnetic features. One key thing about making it is how quickly we cool the material. The laser method we used naturally cools things super-fast, which is great for controlling the structure of our material. We studied how the structure changes with different settings and how it affects the material's magnetic properties.

Acknowledgements

I am deeply grateful to Dr. Lei Zuo and Dr. Hang Yu for their invaluable guidance, unwavering support, and constructive feedback throughout the entirety of this research endeavor. Their expertise, encouragement, and insightful discussions have greatly enriched this thesis.

Furthermore, I would like to extend my sincere appreciation to CEHMS Center via NSF Awards # 1738689 for their financial assistance, the CEHMS IAB association, the associated NSF START Supplement and also the ICTAS EFO Seed Grant program. All these supports enabled me to undertake and complete this research. Their belief in the significance of this work and their investment in my academic pursuits have been instrumental in the realization of this thesis.

I would also like to express my heartfelt thanks to my family, friends, and colleagues for their constant encouragement, understanding, and motivation during this challenging yet rewarding academic journey. Their unwavering belief in my abilities has been a driving force behind the successful completion of this thesis.

Lastly, I extend my gratitude to all the participants and individuals who generously shared their time, knowledge, and experiences for the purpose of this research. Without their contributions, this work would not have been possible.

Table of Contents

List of Figures

List of Table

List of Abbreviations

AM	Additive Manufacturing
L-PBF	Laser based Powder Bed Fusion
SLM	Selective Laser Melting
SLS	Selective Laser Sintering
XRD	X-ray Diffraction
SEM	Scanning Electron Microscopy
EDS	Energy Dispersion Spectroscopy
EBSD	Electron Backscatter Diffraction
VSM	Vibrating-Sample Magnetometer
PPMS	Physical Property Measurement System
MG	Metallic Glass
GFA	Glass Forming Ability
COD	Crystallography Open Database
BD	Building Direction
SVM	Support Vector Machine
MP	Melt Pool
MPB	Melt Pool Boundary

HAZ	Heat Affective Zone
IPF	Inverse Pole Figure
PF	Pole Figure
M_s	Saturation Magnetization
H_c	Coercivity

1. Introduction

Soft magnetic alloys have garnered significant attention over the decades, primarily due to their pivotal role in various applications, including power transformers, electric generators, and, most notably, electric motors [1]. Conventional manufacturing methods typically yield amorphous or polycrystalline forms of these materials, which often require the inclusion of rare-earth elements for use in electric motor applications, adding to their cost. However, recent advancements in material processing techniques have enabled the production of nanocrystalline forms of soft magnetic materials, exhibiting superior magnetic properties. These advancements may potentially reduce the need for incorporating expensive rare-earth elements in specific applications. The remarkable magnetic properties of soft magnetic materials, such as high saturation magnetization, low coercivity, and high flux density, have consistently attracted attention and research efforts in the past. In light of the development of electric motor vehicles and related innovations, enhancing the magnetic properties of materials used in motor cores has become imperative to achieve higher operational efficiency and reduce core losses, including Eddy current and Hysteresis losses. Various strategies, involving different manufacturing techniques, have been explored to fabricate nanocrystalline soft magnetic alloys and demonstrate methods for enhancing magnetic performance.

1.1 Ferromagnetism

Soft magnetic materials exhibit ferromagnetism, which is defined as the spontaneous alignment of atomic magnetic moments, resulting in a strong magnetic field when subjected to an external magnetic field. This alignment allows them to retain magnetic flux permanently. Atomic magnetic moments or spins randomly fluctuate but align in the same orientation within individual

exchange correlation lengths, known as magnetic domains. The alignment of magnetic moments within the same domain is driven by the exchange interaction with adjacent atoms in close spatial proximity. On a quantum scale, magnetic domains are separated and isolated by domain walls. At these boundaries, rotating magnetic moments gradually change their orientations as they transition from one domain to another [2]. Magnetic properties are typically characterized and represented in the hysteresis loop, as shown in Figure 1. In the hysteresis loop, achieving high saturation magnetization and low coercivity is energetically favored for optimized energy efficiency. The area enclosed by the hysteresis loop quantitatively represents hysteresis loss. In general, magnetic performance in applications can be significantly affected by two major energy losses: hysteresis loss and eddy current loss. Hysteresis loss results in energy dissipation in the form of heat due to magnetic anisotropy. Anisotropy can be further categorized into magnetocrystalline anisotropy and magnetostriction anisotropy, which are two major contributing factors. Magnetocrystalline anisotropy can be understood as the resistance encountered during the process of magnetic moments switching their orientations in the hysteresis cycle. This resistance can be attributed to the preferred crystalline orientation within the crystal structure, leading to energy consumption, especially at high coercivity levels induced by anisotropy. The size of the exchange correlation length and structural correlation length plays a role in reducing the impact of magnetocrystalline anisotropy in various conditions. Magnetostriction anisotropy describes dimensional changes in response to the alignment of magnetic moments under a magnetic field. However, the effect of magnetostriction can be minimized through annealing heat treatment after bulk-scale fabrication, making its impact negligible. As for another form of energy loss, eddy current loss affects energy efficiency by inducing eddy currents, which can be explained by Faraday's second law. Changes

in the magnetic field environment of an existing system introduce eddy currents, eventually leading to energy dissipation in the form of heat.

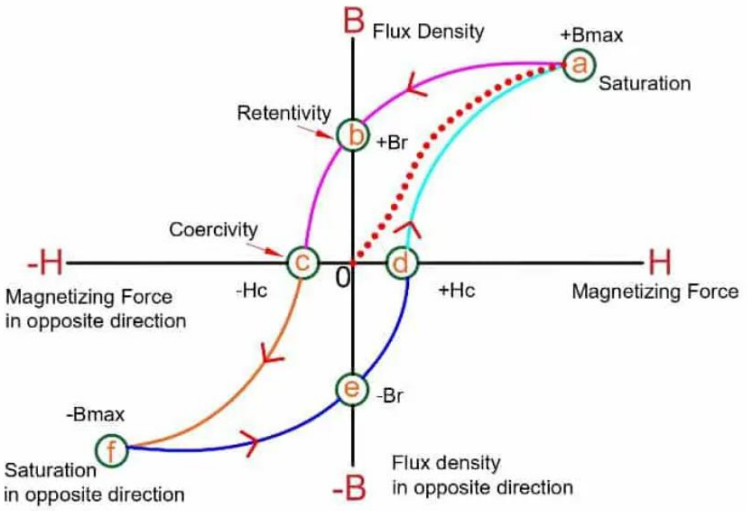

Figure 1: Hysteresis loop of ferromagnetic materials [1].

1.2 Soft magnetic materials

Soft magnetic materials are characterized by their low coercivity. Figure 2 illustrates the variation in compositions of different soft magnetic materials. Among all types of soft magnetic materials, iron-based alloys are prevalent, typically consisting of iron (Fe), silicon (Si), and the metalloid boron (B). These alloys are favored due to their enhanced glass-forming ability and amorphous structural stability [4], [5]. The molar percentage of each element can be adjusted to yield different microstructures and material properties. Given the abundance of iron and silicon on Earth, Fe-Si alloys and unalloyed iron have a significant presence in the soft magnetic materials market. These materials play a crucial role in electrical energy generation and transmission, especially as core materials for electrical cores in modern vehicles. However, one drawback of this

class of materials is related to energy losses in high-frequency applications, where crystalline soft magnetic alloys face challenges, primarily due to Eddy current losses resulting from their limited characteristic magnetic properties. Traditionally, ferrite soft magnetic alloys, such as MnZn and NiZn-based materials, have dominated high-frequency applications. Amorphous and nanocrystalline soft magnetic materials represent a relatively new approach compared to crystalline alloys. The intriguing concept of combining nanoscale grain size and desirable soft magnetic properties challenges the traditional view of crystalline magnetic materials, promising superior magnetic performance with high saturation magnetization and low coercivity [6]. These magnetic properties, including saturation magnetization, permeability, and coercivity, are known to depend on the chemical composition. Additionally, the crystallinity of the parent composition plays a pivotal role in the distribution and orientation of magnetic domains within the material. In recent years, there has been a growing interest in investigating the magnetic properties of amorphous and nanocrystalline soft magnetic materials due to their improvements over conventional crystalline counterparts.

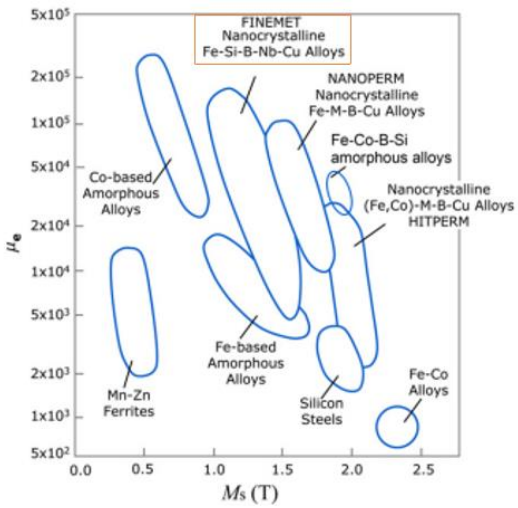

Figure 2: Magnetic property in terms of saturation magnetization and permeability of various ferromagnetic materials/alloys [2].

1.3 Finemet nanocrystalline materials

The enhanced magnetic properties of nanocrystalline materials, such as higher saturation magnetization and permeability coupled with lower coercivity, originate from optimizing the magnetic performance of amorphous alloys. Researchers have attributed the development of nanocrystals in amorphous materials to annealing processes, resulting in an amorphous-to-nanocrystalline transition. Numerous studies and research papers, particularly focusing on Finemet nanocrystalline alloy, have been published over the past decade to improve magnetic performance and understand structural impacts [8]. In principle, embedded nanocrystals can enhance permeability, which is strictly limited by the structural correlation length, or simply put, grain size. As mentioned in the previous section, the motion of magnetic domain walls is driven by exchange interactions between atoms, affecting the motion of magnetic moments generated by electron spins. Consequently, grain boundaries and defects introduce energy barriers, impeding the motion of domain walls. In Dr. T. Gheiratmand's work, the correlation of coercivity with grain size in nanocrystalline soft magnetic alloys was well interpreted, demonstrating a proportional relationship [8].

The superior magnetic performance of nanocrystalline alloys is explained by the exchange softness effect, which mitigates the amplitude of magnetocrystalline anisotropy within the magnetic domains at extremely fine structural correlation lengths [9]. Essentially, this means that exchange interactions among nanocrystalline magnetic domains can overcome the detrimental anisotropic effects observed in larger magnetic domains. Iron-based nanocrystalline alloys have exhibited excellent properties, including high saturation magnetization (~1.5 Tesla), high permeability (~105), and low coercivity. Consequently, lower hysteresis loss (~0.1-0.2 W kg-1) and lower eddy current loss, in comparison to crystalline counterparts, have been reported [6], [8].

Iron-based soft magnetic alloys are predominantly classified into three categories: Finemet with a crystal lattice of DO30Fe (Si), Nanoperm with a crystal lattice of bcc-Fe, and Hitperm Finemet with a crystal lattice of B2-Fe50-Co50 [8]. In this work, our focus is on the Finemet composition to investigate microstructural development using an additive manufacturing technique and to reveal the impact of processing parameters on crystal structure and resulting magnetic properties. Finemet is the commercial name of the nanocrystalline alloy Fe-Si-B-Cu-Nb. Traditionally, Finemet nanocrystalline ribbons exhibit an amorphous structure when as-quenched after fabrication using melt spinning. Subsequent specific heat treatments carefully induce the growth of alpha-Fe phase nanocrystallites, with extraordinarily fine grain sizes ranging from 20 to 100 nm in diameter [9]. Finemet was historically invented by a Japanese scientist, Yoshizawa, and his team in 1988 [10]. Their research group investigated the composition of Finemet nanocrystalline material derived from typical Fe-Si crystalline alloys and noted excellent magnetism with super-fine crystallites in nano-size.

In essence, during the initial stages of solidification, body-centered cubic (bcc) α-Fe (Si) nanocrystals nucleate around Cu atoms, acting as nucleation sites that promote the formation of nanocrystals embedded within the amorphous matrix. Nb atoms inhibit the coarsening (grain growth) of nanocrystals due to their giant atomic size, stabilizing them within the amorphous matrix [11]. Among the many scientific studies on the nanocrystalline kinetics of the Finemet alloy, the structure of the FeSi phase can be significantly affected by the presence of Si content in the Fe unit cell during the solidification process. The experimentally generated Fe-Si phase diagram, as shown in Figure 3, suggests the transition from a disordered bcc α-Fe (Si) structure to an ordered D03 α"-Fe (Si) structure when the Si content exceeds 12.9 atm% in the metal matrix [8]. Evidence of this phenomenon is also supported by research from D.S. dos Santos's group, which revealed

the crystallization kinetics of Fe-B-Si-based ferromagnetic materials at dynamically adjusted annealing temperatures. Figure 4 illustrates the evolution of diffraction amplitude as a function of annealing temperature, schematically demonstrating the initial formation of α-Fe (Si) with slight diffraction of the Fe3B phase. Subsequently, the metastable boride Fe3B is gradually replaced by the stable formation of Fe2B phase at elevated temperatures [12], [13]. Combining the phase diagram and crystallization kinetics, it is reasonable to conclude that the solubility of Si increases proportionally with the level of thermal environment. Thus, when the solubility of Si surpasses the threshold, more Si atoms are likely to distribute within the Fe unit cell, encouraging this phase transition. Observations of the evolution of the metal matrix are also visible and will be discussed.

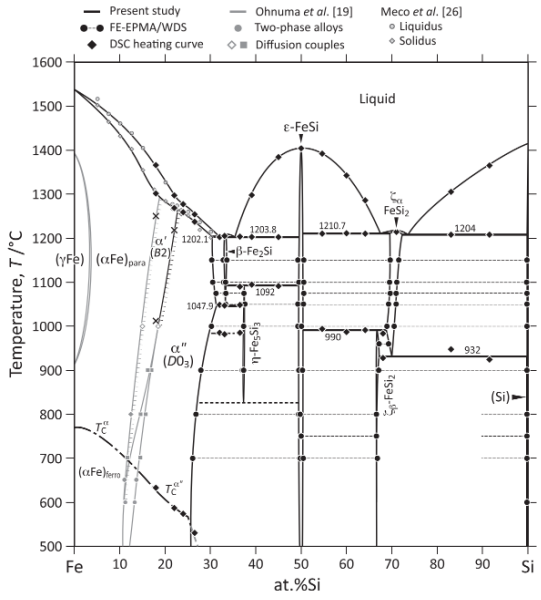

Figure 3: Experimentally interpreted Fe-Si phase diagram shows the disordered-ordered transition of ferrite. [3].

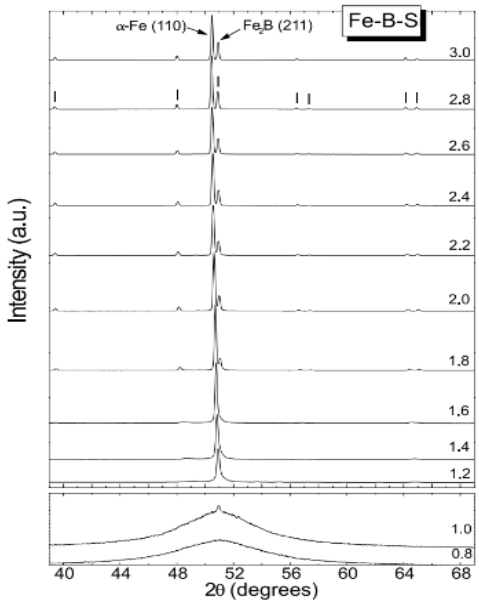

Figure 4: Crystalline phases evolution of FeBSi alloy in XRD at elevating annealing temperature. [4].

1.4 Conventional Manufacturing techniques

Conventional manufacturing techniques for Finemet nanocrystalline alloys rely on the melt spinning process, followed by annealing as a crucial step to achieve the desired microstructure, as explained earlier. Typically, Finemet alloy ribbons have a thickness of around 20 μm. This thickness allows as-quenched Finemet alloy ribbons to experience an extremely high cooling rate of approximately 10^6 to 10^7 K/s [15]. Due to this exceptionally high cooling rate during solidification, there is insufficient time for crystallites to form large clusters or agglomerate into grains. Instead, they randomly align with each other without a preferred orientation, resulting in the amorphous phase. To achieve a microstructure with embedded nanocrystals within the amorphous matrix, an annealing process is conducted for approximately 1 hour at temperatures ranging from 600 to 800 degrees Celsius on the as-quenched amorphous alloys. This annealing

facilitates the formation of alpha Fe-Si, Fe3B, and Fe2Si phases within the amorphous matrix [10]. However, since nanocrystallites are highly sensitive to the thermal environment, grain growth can easily occur under specific conditions. Heat treatment, such as annealing, effectively promotes the grain growth of nanocrystals within the existing amorphous matrix. While the thermal gradient predominantly controls the microstructure and grain growth during solidification, the chemical composition of Finemet alloys can also play a vital role in governing microstructural changes. In reality, within the market for nanocrystalline soft magnetic materials, the consensus is that advantages can be gained from the inclusion of noble elements (e.g., Cu, Ag, Au, etc.), which enhance the nucleation of the body-centered cubic (bcc) matrix. Additionally, early transition metal elements (e.g., Zr, Nb, Hf, Ta, etc.) can impede the crystalline growth of nanocrystalline materials under devitrification conditions [16]. The commercial manufacturing technique for producing Finemet nanocrystalline alloys has been primarily centered on melt spinning, as shown in Figure 5, for years due to the strict requirement for an extreme quenching rate [4]. However, in principle, Finemet nanocrystalline alloys can be processed using various manufacturing techniques, including both traditional and additive methods. These methods may involve rapid quenching after casting, mechanical alloying, plasma spray, friction stir deposition, direct energy deposition, and more. Achieving precise control over amorphous and nanocrystalline phases is crucial, as it presents technical challenges for most of the techniques mentioned above []. Furthermore, research has demonstrated that bulk-scale metallic glasses exhibit different magnetic performance characteristics compared to melt-spun ribbons [17]. Thus, successfully fabricating bulk-scale Finemet alloys with the expected nanocrystalline microstructure to achieve outstanding magnetic properties represents a significant milestone in additive manufacturing (AM). On the other hand,

traditional fabrication techniques have limitations when it comes to bulk-scale production, mainly due to dimensional constraints and low ductility, which have always been challenging aspects [18].

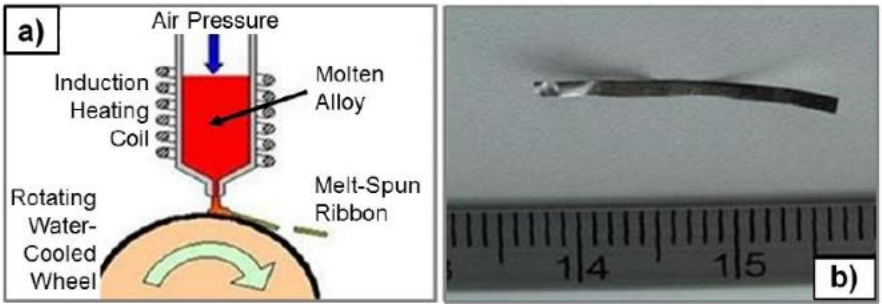

Figure 5: Melt Spinning traditional manufacturing technique to fabricate Finemet alloy ribbons possess amorphous matrix. [5].

1.5 Additive Manufacturing techniques

The advancement of metal additive manufacturing (AM) has matured considerably and can be understood as a bottom-up manufacturing technique that offers the freedom to design near-net shapes for complex parts, which would otherwise require a significant amount of work using traditional manufacturing methods. Additionally, parts fabricated using AM exhibit promising mechanical and functional qualities when proper parameters are optimized, which has garnered significant interest in replacing traditional fabrication techniques for Finemet nanocrystalline alloys with AM. Extensive research has been conducted on similar compositions of iron-based amorphous and nanocrystalline alloys using various AM techniques for various purposes. One such laser-based metal AM technique is the Laser Powder Bed Fusion (L-PBF), also known as Selective Laser Melting/Sintering (SLM/SLS), which has been used for iron-based soft magnetic

materials for a decade, as shown in Figure 6. For example, starting with the basic Fe-Si soft ferromagnetic alloy, Garibaldi's group has been researching the metallurgy of high-silicon steel Fe-Si (6.5-6.9 wt%) fabricated by SLM and how annealing affects the microstructure and magnetic performance. They have also investigated the correlations under different processing parameters, including laser power, scanning speed, and scanning strategy [20]. Dr. Shen's group has studied the morphological impact of different cooling rates at the same laser power on the Heat-Affected Zone (HAZ) around the bottom of melt pools for Zr-based metallic glass (MG) [21]. Dr. Zrodowski's group has reported that scanning strategies can manipulate the Glass Forming Ability (GFA) of Fe-Si-B-Cr-C MG due to the sophisticated temperature gradient within the melt pool [22]. Dr. Gheiratmand's group has researched the crystallization mechanism and the impact of key elements on the magnetic performance of nanocrystalline SMG materials [8].

To demonstrate the feasibility of SLM in processing Finemet nanocrystalline alloy, one of the most critical factors to address is achieving the necessary cooling rate, which typically falls in the range of 10^5 - 10^7 K/s [15]. Meanwhile, the amorphous phase may not survive the Heat-Affected Zone (HAZ) during bulk-scale processing, but at the very least, the grain structure should not experience significant growth. SLM offers an environment that meets the basic requirement for approaching a nanocrystalline structure, with reported cooling rates ranging from 10^2 - 10^{12} K/s [23]. Considering the solidification process of the Finemet alloy involves three metallic phases under complex thermal conditions, solidification microstructures corresponding to different phases are governed by critical factors such as temperature gradient (G), solidification rate (R), and undercooling. These factors lead to various microstructure morphologies, including cellular, planar, columnar, equiaxial, and dendritic shapes, as shown in Figure 7. The gradient-to-solidification ratio (G/R ratio) describes the solidification morphology, while the product of G and

R indicates the cooling rate [24]. Consequently, differences in morphology can be observed across the melt pool structure. Generally, in the academic field of SLM fabrication of Finemet nanocrystalline alloys, the lack of in-depth research to uncover the correlation between processing parameters and the mechanism of nano-crystallite growth has hindered progress toward industrial-scale production of products such as electric motors and power generators made from Finemet nanocrystalline alloys.

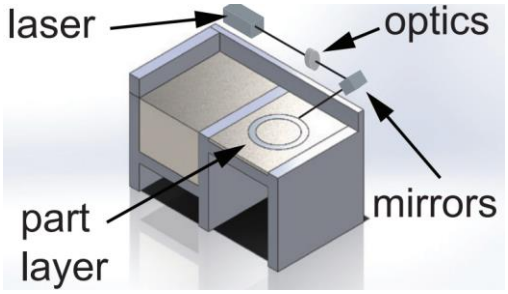

Figure 6: Illustration of selective laser melting process [6].

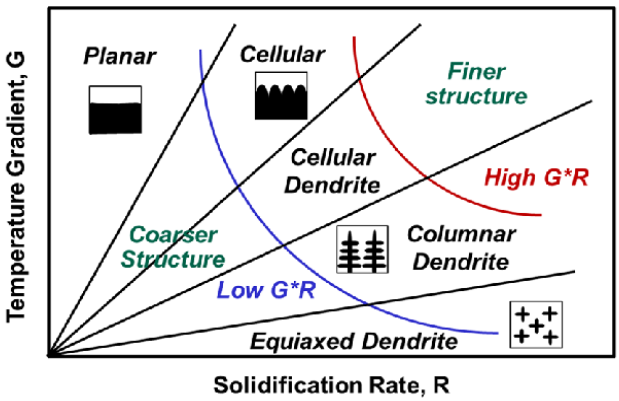

Figure 7: Solidification mechanism of metal alloy as a function of temperature gradient and solidification rate, with respect to different solidified morphologies [7].

1.6 Defects formation

The Laser Powder Bed Fusion (LPBF) additive manufacturing (AM) technique has been extensively explored in academia for optimizing processing parameters and enhancing mechanical and functional properties. Defects in LPBF can be broadly categorized into two types: cracks and pores. Crack formation is primarily driven by residual stress, which breaks metallic bonds to achieve a more thermodynamically preferred state. Pores can be further classified into two structural features: lack of fusion holes and keyholes. Lack of fusion holes are typically found under conditions of low laser power and high scanning speed, resulting in relatively large-scale features compared to keyholes. Hatch spacing, the distance between hatch lines, also plays a crucial role in governing the overlap of melt pools to ensure that the laser completely melts powders at each layer. Lack of fusion holes are formed along with un-melted powders, exhibiting random features that are visible under optical microscopy. The presence of a large number of lacks of fusion holes can severely impact the universal criteria for justifying the bulk-scale density of as-printed samples, consequently significantly affecting mechanical properties. On the other hand, the formation of keyholes is a well-known byproduct of complex fluid dynamics in the liquid state. The applied laser provides sufficient power to vaporize the material powder, generating a back recoil pressure that drives the liquid in the opposite direction of the laser interaction. By increasing the laser power, the back recoil pressure can open up a deep and thin vapor depression with a high aspect ratio. Spherical micro-scale air bubbles can become trapped at the bottom of the keyhole depression due to the extreme quenching rate. Dr. Huang's group utilized synchrotron X-ray imaging to investigate the initial formation of keyhole porosity at the transition regime, along with the preferred collapse position and the mechanism of air bubble formation during the morphological changes of keyholes [26]. Defect formation corresponding to parameter

optimization, including hatch spacing, rotating angle, layer thickness, laser power, and scanning speed, will be discussed. Additionally, metal matrix and nanocrystallite formation and size will be characterized and calculated. Techniques such as X-ray diffraction (XRD), Scanning Electron Microscopy (SEM) imaging of grain structure and size with respect to various processing parameters will be revealed, and Energy Dispersion Spectroscopy (EDS) will be used to examine chemical composition. Finally, Electron Backscatter Diffraction (EBSD) will explain the preferred crystallite orientation on the cross-section and top surface of the as-fabricated Finemet nanocrystalline alloys.

2. Experiment procedure

2.1 Material powder

The crystalline soft magnetic material powder was supplied by Tianjin Leads Technology Co., China. It possesses the typical chemical composition of commercial Finemet nanocrystalline material, which consists of Fe73.5Si13.5B9Cu3Nb1 (at. %). This Finemet material powder was produced using the gas atomization technique, which results in an extremely high quenching rate. In this process, droplets of the material are dispersed in the air, and solidification occurs during free fall. This process gives rise to the distinctive spherical shape of the Finemet material powder, as depicted in Figure 8. The image captured using the JEOL 300 Scanning Electron Microscope (SEM) not only showcases the morphological features of the material powder but also reveals the size distribution, which ranges from 5 μm to 80 μm. This size distribution is well-suited for use in SLM machines. Throughout the experiment, the powder has been continuously reused. After the recycling process, which involves sieving through a 65–70 μm-sized sieve provided by W.S. Tyler Co., morphological defects become observable under SEM. Factors such as collisions, melting, stretching, and elongation are consequences of the laser sintering process (with no phase transformation occurring) and laser spattering (where powders are blown away). Consequently, potential cracks and pores could be induced due to the uneven distribution of laser energy on the irregularly shaped powder. The X-ray diffraction (XRD) pattern of the material powder, obtained using the Rigaku Smart Lab XRD, is displayed in Figure 9. The presence of background noise in the XRD data is more pronounced due to the uneven surfaces of the material powders. Nevertheless, non-amorphous features are evident from the existence of strong and sharp peaks of α-Fe (Si) and Fe3Si. Although the Fe2B phase exhibits a low intensity and is somewhat hidden within the

background noise, it can still be detected. Based on the XRD characterization of the material powder, it can be concluded that the Finemet powder fabricated via gas atomization in our research does not exhibit amorphous features, as might be expected under extremely high cooling rates. The XRD peaks align well with the Crystallography Open Database (COD), confirming the presence of metal matrix phases.

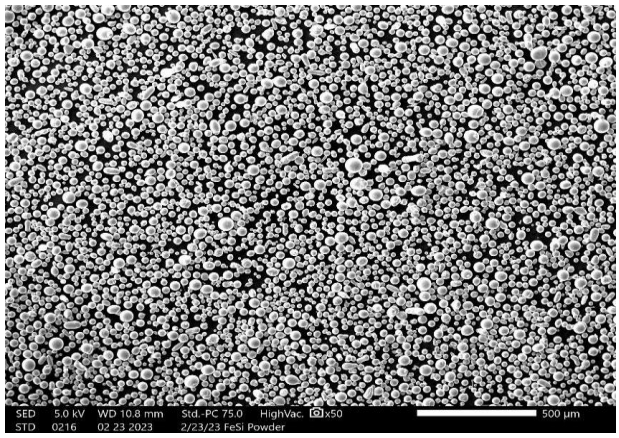

Figure 8: Low magnitude of SEM image of Finemet alloy powder.

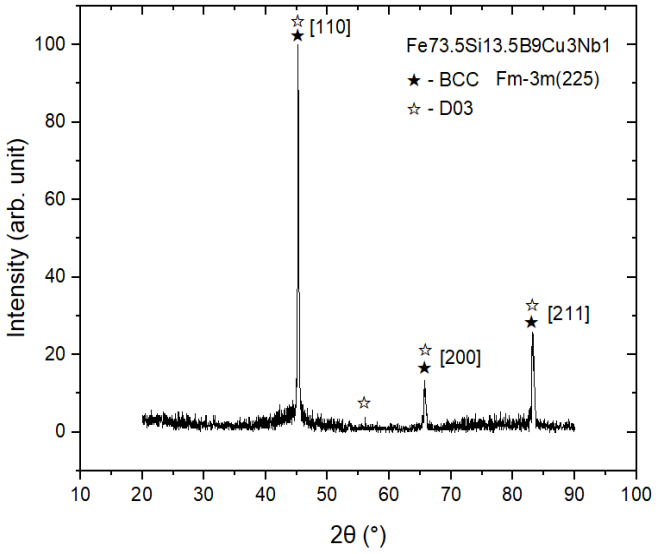

Figure 9: XRD characterization of Finemet alloy powder.

2.2 Processing parameters

In this research study, we utilized the PANDA selective laser melting machine from Open Additive Co. The machine comprises three main components, as illustrated in Figure 10. The first component is an isolated chamber that is filled with shielding gas, typically argon and nitrogen, supplied by Cryogenic Gas Co. These gases are commonly used to create the desired atmosphere within the chamber. The second component is a powder catcher chamber designed to collect waste or used powders generated during the printing process. Aside from the main body of the machine, there is a tank of liquid shielding gas connected to it. This tank continuously supplies gas into the chamber during the printing process to maintain the desired environment. The manufacturing parameters encompass both geometric and functional parameters. Geometric parameters, as depicted in Figure 11, include layer thickness, hatch spacing, angular rotation, scanning strategy, and sample morphology. These factors influence the physical dimensions and shape of the printed object. Functional parameters, on the other hand, encompass laser power and scanning speed. These parameters play a pivotal role in controlling the thermal gradient and melt pool morphology, which are critical for manipulating microstructural features.

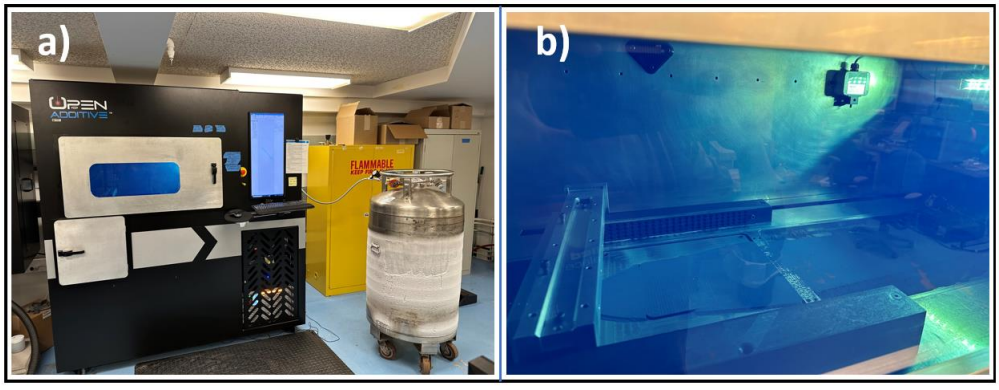

Figure 10: a) ‘PANDA’ SLM machine from OPEN ADDITIVE Inc.; b) recoating process.

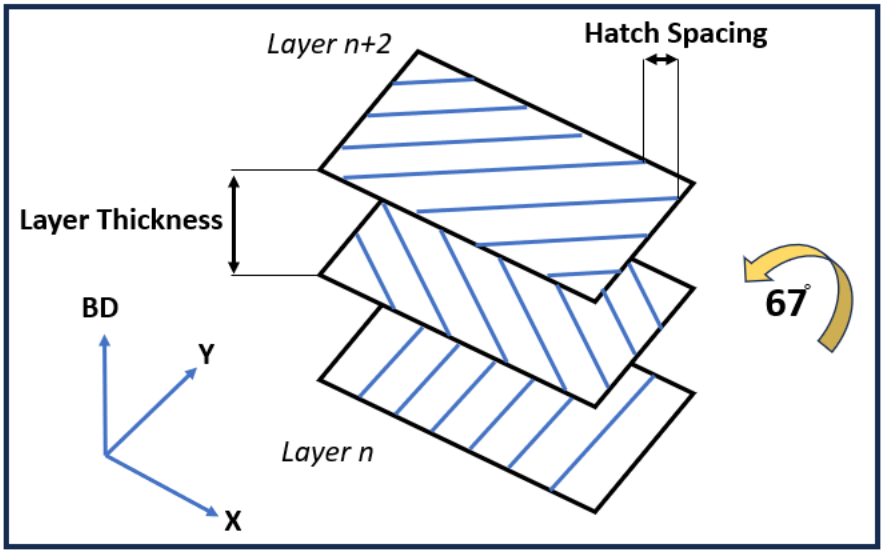

Figure 11: Schematic image of geometric processing parameters including layer thickness, hatch spacing, angular rotation and scanning direction.

2.2.1 Layer thickness

The layer thickness was determined based on the powder size distribution and considerations related to the cooling rate. Conventional manufacturing of melt-spun Fe73.5Si13.5B9Cu3Nb1 (at. %) alloy ribbons typically result in thicknesses ranging from 15 to 25 µm. Such thickness, combined with the rapid spinning process, provides sufficient cooling rate to facilitate the formation of the amorphous phase. To achieve a similar cooling rate during the Selective Laser Melting (SLM) fabrication process, we initially set the layer thickness to approximately 20 µm. However, upon characterizing the powder size distribution, which ranged from 5 to 80 µm with an average around 45 to 50 µm, it became apparent that restricting the layer thickness to 20 µm was no longer practical. Larger powder particles (greater than 20 µm) were being displaced during the recoating process. Additionally, powder spattering, which includes un-

melted powders being blown away by ambient gas flow and droplet spattering directly ejected from the melt pool outside the build area, contributed to a decrease in powder layer thickness of at least 15% to 20%, making the realistic powder layer thickness even less than the initially expected value [27]. As a result, we adjusted the layer thickness to 50 μm. Furthermore, the cross-bed flow design, which was intended to reduce the impact of spattering issues, also had the added benefit of enhancing the cooling rate.

2.2.2 Hatch spacing

Hatch spacing refers to the linear distance between the laser focusing spots of two adjacent melt pools. Properly selecting and optimizing hatch spacing is crucial for achieving high-quality and mechanically sound as-printed components. Broad hatch spacing can lead to voids caused by a lack of fusion, while overly narrow hatch spacing, which induces extremely high thermal gradients, can increase crack density and porosity. Therefore, achieving a balanced hatch spacing, in conjunction with laser power and scanning speed, is essential for improving as-printed density and eliminating the powder leveling height differences caused by powder denudation. Powder denudation is a phenomenon where powders are blown away by the surrounding gas flow of vaporized material powder at regular ambient gas pressure in the chamber. Dr. Matthews's group conducted a detailed study that focused on the physics behind the denudation mechanism, particularly in the context of Ti-6Al-4V [28]. The width of the denudation zone was reported to range from 100 to 200 μm for laser power inputs ranging from 150 W to 200 W. In addition to determining the hatch spacing, the size of the melt pool is another significant factor that requires careful consideration. Melt pool size is directly proportional to the laser energy. For instance, at 180 W of laser energy, the melt pool width for Finemet alloy was measured to be in the range of

100 to 130 μm. To avoid defects related to a lack of fusion, it is important to leave at least ⅓ to ¼ overlap between adjacent melt pools. Consequently, a hatch spacing of 90 μm was chosen for all samples, as it represents an intermediate state that takes all of these considerations into account.

2.2.3 Angular rotation

The angular rotation between each layer was set at 67°. It's important to note that the choice of angular rotation can vary depending on the specific requirements of the as-printed parts. Classical rotation angles of 45°, 90°, 67°, and 105° can all be implemented in the Selective Laser Melting (SLM) fabrication process. However, it's crucial to consider how geometric parameters, especially angular rotation, can significantly impact surface finish and functional property anisotropy [29]. For example, surface roughness can induce residual stress within the bulk material, which may necessitate additional heat treatment or mechanical machining steps to meet industrial standards. Research has shown that an angular rotation of 67° between each layer effectively enhances bulk-scale isotropy and reduces surface roughness. Dr. Dimter's group has provided a comprehensive explanation of this theory [30]. In terms of the melting process, an angular rotation of 67° ensures that there is no repeating laser track between each layer throughout the entire printing process. This minimizes concerns related to uneven surfaces and lack of fusion at certain spots on the powder bed. The thermal gradient underlying each layer and individual tracks results in thermal-induced stress during deposition. Initially, the heat flow from melted materials onto the already deposited layers generates compression stress, consolidating the solidified part on the bottom. Subsequently, a constraint mechanism occurs at the top of the solid part due to the mismatch of cooling rates across the body, leading to tensile stress [29]. Furthermore, the phenomenon of the laser driving melted metal from the edge of the laser trail towards the center

of the laser track is primarily attributed to thermocapillary forces. This force arises from changes in surface tension during the melting process. Since melted metal experiences an extremely high cooling rate along the laser trail, a steep temperature gradient forms, resulting in differences in surface tension and the generation of capillary streams. Using a non-repeating laser track by applying a 67° rotation ensures that the solidified bulk materials are randomly oriented along the building direction (BD)

2.2.4 Scanning strategy and bulk-scale morphology

A bi-directional scanning strategy was employed in this research study, primarily to ensure crystalline isotropy. The bulk-scale samples were designed as cylinders. The scanning strategy plays a crucial role in controlling surface roughness and material humping in Laser Powder Bed Fusion (L-PBF) processes. When the laser interacts with the material powder, it vaporizes the powder at high energy, generating a high-pressure plasma that encounters the melted material, subsequently creating a recoil pressure in the opposite direction of the laser's travel path. In the complex fluid dynamics of the melt pool in the Selective Laser Melting (SLM) technique, various forces, including capillary force, Marangoni force, buoyancy forces, and additional recoil pressure, significantly impact melt pool structures. Among these forces, recoil pressure can have a drastic effect, typically an order of magnitude greater [31]. Recoil pressure behavior varies depending on laser power. With relatively low power, thermal energy is transferred in conduction mode, which may not fully melt the material powder and can result in lack of fusion defects. Conversely, high laser power induces a stronger recoil pressure, allowing for heat convection to melt the material powder but also increasing the likelihood of generating keyhole effects [31], [32]. Recoil pressure is a governing factor in causing material humping, especially during welding and L-PBF processes.

At relatively low cooling rates, recoil pressure periodically drives melted metal to agglomerate together and solidify. Dr. Seiler's group has elucidated this theory well, taking into account surface tension and back recoil pressure [31]. By using the bi-directional scanning technique, ideally, melted metal will be more evenly distributed along the laser tracks, even in the presence of recoil pressure. Additionally, bi-directional scanning can significantly enhance efficiency by halving the laser's traveling path.

The choice of cylindrical sample morphology was made with great care. Delamination and warping are two prominent flaws that can lead to printing failures during fabrication, both stemming from extreme thermal gradient-induced stress. Maintaining a stable thermal environment and evenly distributing heat across the layer are crucial to addressing thermal-induced stress defects. During the scanning process, the laser emitter always possesses angular momentum. Therefore, precise control of the laser emitter requires applying momentum in the opposite direction to ensure that the laser pauses at the fixed position. Consequently, negative acceleration serves as the counterpart. This leads to an increase in thermal gradient along shorter laser travel paths at the edges, accumulating more heat over the same distance compared to longer laser travel paths in the middle of the sample. Given the 67° angular rotation of the samples, a spherical top surface was chosen to reduce the difference in travel path distances across the layer. As a result, the difference in thermal gradient is effectively minimized, helping to prevent delamination and warping defects.

2.2.5 Laser power and scanning speed optimization

Laser energy density, calculated as laser power divided by scanning speed and having units of J/m, provides a comprehensive overview of the target processing parameters. This approach was inspired by Dr. Garibaldi's research group, which investigated the metallurgical mechanisms of Fe-Si fabricated using the SLM technique [20]. In this research study, we conducted five successful experiments to optimize processing parameters. The first two sets of experiments involved fabricating samples at laser energy densities of 60, 120, 180, 240, and 300 J/m, with laser power set at 120, 150, and 180 W. The scanning speed was adjusted accordingly. In these initial experiments, three samples from each extreme energy density (60 J/m and 300 J/m) failed due to severe warping issues that hindered the recoating process. As a result, the third experiment focused on energy densities of 120, 180, and 240 J/m, in combination with laser powers of 60, 90, 270, and 360 W. This broader range of laser powers aimed to explore more possibilities and bridge the gap in laser power variation corresponding to scanning speed.

After the first three experiments to fine-tune the printing parameters, several noteworthy conclusions were drawn. It was observed that Finemet metal alloy can indeed be fabricated using an SLM machine with acceptable as-printed quality in terms of porosity and crack density. Laser powers not exceeding 240 W, and preferably above 120 W, increased the likelihood of successful bulk-scale fabrication. Interestingly, the same laser energy density did not yield similar as-printed quality for different combinations of laser power and scanning speed. Therefore, laser energy density was narrowed down to three values: 120, 180, and 240 J/m. However, further verification was required for the laser power variation corresponding to different laser energy densities, especially considering the initial 30 W difference.

For a comprehensive examination of laser power and to fill gaps in the database for each set of laser energy densities, each energy density set should include at least one sample with laser power ranging from 60 W to 240 W. Thus, the fourth experiment served as a supplementary test to systematically explore unknown processing parameters. Figure 12 illustrates the distribution of processing parameters in relation to laser energy density. As-printed sample quality was evaluated based on macro-scale porosity and crack density, revealing distinct differences within the extensive sample pool. An initial quality filter was applied to all as-polished samples at the same level. Four promising samples were selected, each representing good quality without a linear relationship between processing parameters: 180 W - 0.75 m/s, 180 W - 1 m/s, 180 W - 1.5 m/s, and 240 W - 1.33 m/s. These targeted samples formed a triangular area encompassing all good samples. The highest quality, with no clear lack-of-fusion defects, was consistently achieved at 180 W - 1 m/s. To confirm the feasibility of this target area and demonstrate the repeatability of good-quality samples from previous prints, the fifth set of printing parameters was generated. We made adjustments with 15 W laser energy differences and 0.125 m/s scanning speed variations, building upon the foundation of 180 W - 1 m/s. The result of the fifth experiment was the absence of failed samples in terms of bulk-scale fabrication. While the as-printed quality did not exhibit complete consistency, decent samples were obtained in the latest printing. With all data points plotted, we employed a Support Vector Machine (SVM) for classification to determine the boundary of the processing window based on as-printed quality.

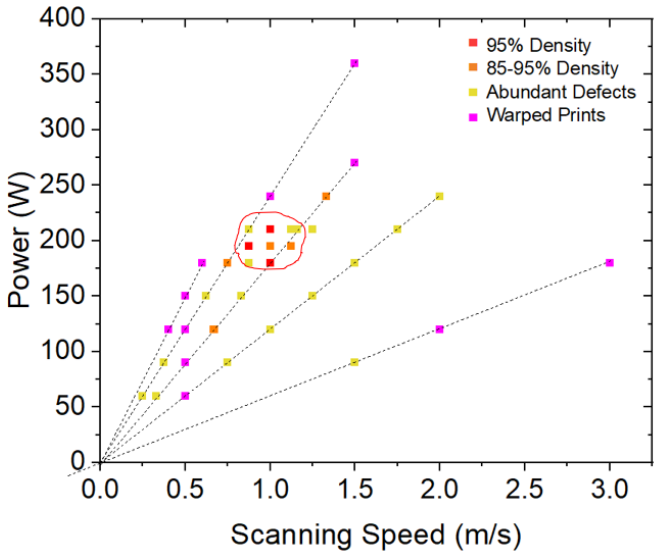

Figure 12: Process parameters optimization, dash line represents different laser energy density input, highlighted boundary elucidates decent as-printed density by the SVM machine learning strategy.

2.3 Characterization methods

After optimizing the processing parameters, nine samples with relatively high bulk-scale density were selected for advanced characterization to unveil microstructural features and perform VSM magnetic characterization. The selected samples encompassed various comparison groups: those with a laser energy density of 180 J/m but different combinations of laser power and scanning speed, samples with fixed laser power (180 W and 190 W) but varying scanning speed, and samples with a fixed scanning speed of 1 m/s while adjusting the laser power from 180 W to 210 W. This approach allowed for comprehensive and scientifically rigorous characterization analysis, covering bulk-scale density, crystalline structure, melt pool morphology, metal matrix, crystalline texture, and magnetic properties. To prepare the samples for characterization, a wire EDM

machine was employed to machine them along the build direction (BD). Crystalline phases of the bulk-scale Finemet alloy were characterized using Rigaku SmartLab and Rigaku Miniflex X-ray diffraction machines with Cu radiation (λ = 1541 Å). Results from the XRD analysis were then applied to Scherrer's equation to calculate and analyze the trends in crystallite size. Before optical and electron microscopy imaging, the samples were etched using a 5% Nital etchant (5% HNO3 + 95% Ethyl Alcohol). The etching time varied depending on the individual samples, with higher-density samples requiring 2-3 minutes of etching and lower-density samples requiring 1-2 minutes until the melt pool features were clearly visible under the lens. Optical microscopy imaging was conducted using a Nikon Brightfield microscope, followed by Archimedes density characterization. Scanning electron microscopy (SEM) images were captured using the JEOL 300 cryo-electron microscope, and Electron Backscatter Diffraction (EBSD) images were taken with the TESCAN MIRA 3. To assess the magnetic properties, a Vibrating-Sample Magnetometer (VSM) was employed, and hysteresis loops of the samples were generated using the Physical Property Measurement System (PPMS) DynaCool machine.

3. Results and discussion

3.1 Optical microscopy of melt pool morphology and defect

The primary step in sample characterization, aimed at assessing overall defects such as crack density and porosity, involves optical microscopy. After undergoing polishing and etching processes, the as-fabricated samples efficiently reveal the melt pool structure inherent to the Selective Laser Melting (SLM) process. Given that the metal matrix of Finemet alloy consists of three primary phases: α-Fe (Si), Fe3Si, and Fe3B, distinct morphological differences and variations in spectral distribution become visible. These structural features are essential for identifying specific areas on the cross-section, serving as targeting points for more detailed microstructure characterization using higher-level facilities like SEM. Nikon's brightfield optical microscopy offers a range of lenses, from 5x to 100x, with the highest resolution reaching around 0.2 µm. Therefore, images at 5x, 20x, and 100x magnifications were captured to gain a fundamental understanding of the as-printed qualities of etched samples produced under various processing conditions. In Fig 13, it can be observed that samples fabricated at a laser energy of 180 W with varying scanning speeds exhibit large pores and high porosity in the sample produced at the highest scanning speed of 1.5 m/s. Reducing the laser scanning speed significantly decreases pore size. However, lower scanning speeds generate higher laser energy density, making micro-cracks propagating through micro-pores more visible. In Fig 13b, 13c, and 13d, three samples were produced at 195 W with different scanning speeds. The sample with the highest as-printed density is found at the higher scanning speed compared to the other two samples. When considering these two sets of comparison groups, it becomes evident that samples with higher as-printed quality tend to cluster around a laser energy density of 180 J/m³. However, individual samples exhibit distinct defect morphologies that cannot be solely attributed to energy density as the contributing factor.

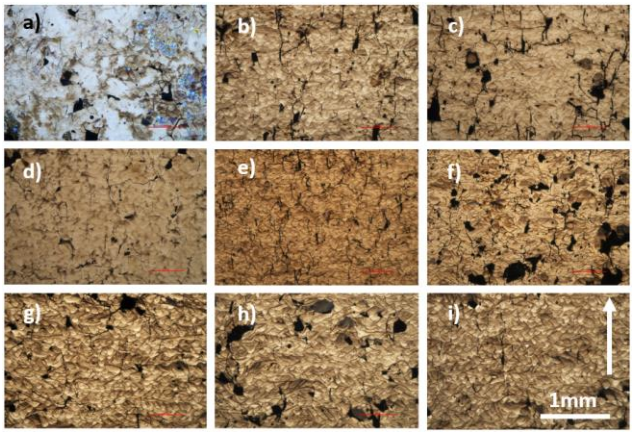

Figure 13: Optical microscopy at low magnitude, to analysis the overall defect formation and crack density; a) 120W-0.67m/s, b) 210W-1m/s, c) 240W-1.33m/s, d) 180W-0.75m/s, e) 180W-1m/s, f) 180W-1.5m/s, g) 195W-0.875m/s, h) 195W-1m/s, i) 195W-1.125m/s.

Aside from defects, molt pool width and length at each layer coherently produce the expected feature. Since during the printing process, layer thickness was set to be 50 µm and hatch spacing was set to be 90 µm. By having high laser energy varies from 120 to 240 W, ⅓ to ¼ of overlap on the edge of melt pool would be expected to avoid lack of fusion defects (material power remain un-melted and leave space in between layers).

Under a 20x lens in optical microscopy, the width and depth of melt pools were characterized using computer software and were found to vary from 90 µm to 140 µm in width and 40 µm to 100 µm in depth. At higher magnifications, the morphological differences in melt pools can be illustrated through the presented spectrum. The Finemet alloy contains multiple metallic phases that react simultaneously with the Nital etchant at different rates. As a result, the melt pool structure is represented by black dots on the melt pool boundary. However, this feature does not form uniformly throughout the melt pool structure. For instance, the brighter/white-

colored region mainly solidifies at the bottom of the melt pool. The mixing behavior between black dots and the brighter region can also be observed, likely driven by the heterogeneous nature of fluid dynamics during solidification. Due to the SLM machine's exceptionally high quenching rate, the morphology resulting from fluid dynamics is frozen before the mixing process is completed.

Individual melt pools exhibit unique features in the metal matrix. Switching from a 20x to a 100x microscope lens, the highest resolution and magnification reveal an additional phase embedded in the metal matrix. In Fig 14, all three samples in the 195 W comparison group display three different phases characterized by morphological differences. The dominant bright-colored metal matrix is homogeneous throughout the entire melt pool, while dots dominate the top of the melt pool. There is also a small amount of grey area with arbitrary morphology observed at the very bottom of the melt pool, more frequently occurring at the overlap area of two to three melt pools. The flowing feature of dots is believed to be driven by Marangoni convection, which involves circulating and outward liquidus flow within the melt pool.

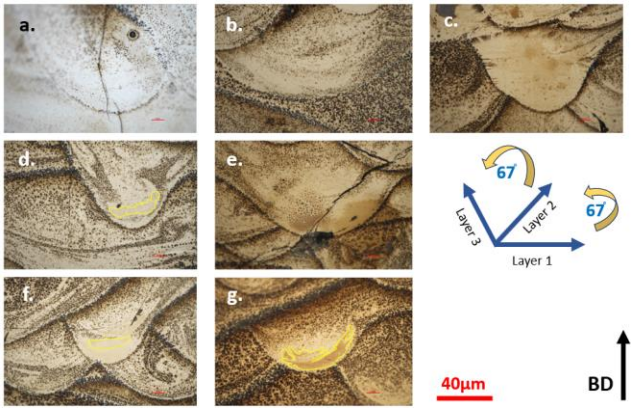

Figure 14: High magnitude of the single melt pool at different processing parameters; a) 180W-0.75m/s, b) 210W-1m/s, c) 180W-1.5m/s, d) 195W-0.875m/s, e) 180W-1/s, f) 195W-1/s, g) 195W-1.125m/s.

Based on the process parameter optimization and subsequent characterization, it can be summarized that among the nine samples that were selected for advanced characterization, the samples produced with laser energy densities around 180 J/m³, specifically 195 W - 1.125 m/s and 180 W - 1.00 m/s, exhibited the least defects in terms of pore density and crack presence. However, it's worth noting that not all samples with a laser energy density of 180 J/m³ showed decent as-printed quality. Pore density and size distribution, along with the presence of cracks, were observed to propagate homogeneously through the cross-section of the samples. Additionally, some local pores were found even in the high-density samples. On the other hand, samples produced at elevated laser energy densities above 200 J/m³ exhibited cracks coexisting with a large number of pores, while relatively large pores were more visible in samples with lower laser energy densities below 150 J/m³.

3.2 Archimedes' density measurement

The bulk-scale density of the nine samples with optimized processing parameters at the as-printed condition is depicted in Figure 15. This representation shows how bulk-scale density varies concerning laser power and scanning speed, creating a counter plot of density with respect to these factors. The counter plot illustrates a trend of a proportional relationship between bulk-scale density and laser power/scanning speed. However, the threshold for laser energy and scanning speed remains within the expected process window established during the parameter optimization. In the counter plot, the red and blue arrows indicate the trends for recommended high and low bulk-scale density. The transition area in between aligns with expectations. It's important to note that, despite the general trends, repeatability should be carefully considered. For instance, in this experiment, two samples with the same laser power and scanning speed (180W-1m/s) exhibited

slightly different bulk density and saturation magnetization. This highlights that detailed parameter optimization cannot be solely simplified by using laser energy density as the only contributing factor. Furthermore, Figure 15b illustrates the relationship between relative bulk-density and laser energy density input. Samples with relative bulk-density greater than 95% are within the range of 180 J/m² to 240 J/m², while samples with relative bulk-density higher than 97% are represented by the conditions of 180W-1m/s and 210W-1m/s. To achieve desired nano-crystals and enhance the magnetic properties of nanocrystalline ferromagnetic materials, it's crucial to carefully control and optimize the processing parameters.

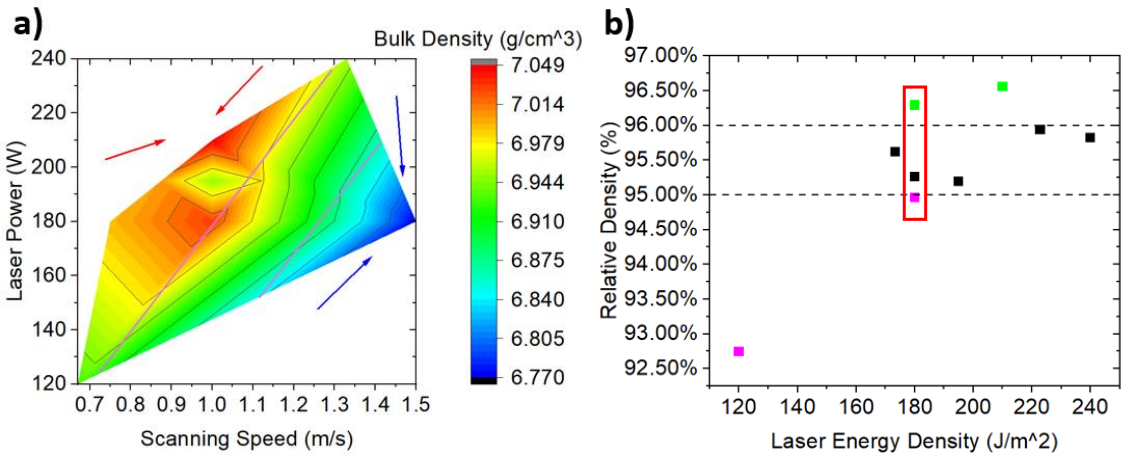

Figure 15: a) Counter plot of bulk -scale density characterized by Archimedes' density measurement, b) Relative density of as-printed parts with respect to laser energy density.

3.3 XRD and peak broadening

To demonstrate the existing crystalline phases and to reveal the trend of peak broadening, it is more significant to understand the impact of processing parameters on crystalline structure

using the Scherrer's equation. XRD patterns for the precursor FINEMET powder and the SLM-processed samples are shown in Fig. 16. The patterns are noisier than usual due to the well-known fluorescence effect exhibited by Fe-containing compounds when irradiated with a Cu X-ray source. This may be understood as a resultant micro absorption effect leading to the element's characteristic X-ray emission regardless of the incidence angle. The comparison of the crystalline precursor FINEMET powder XRD with one of the printed samples is illustrated. The powder sample has a more pronounced fluorescence effect adding to the background. Another important difference is the evolution of the α-FeSi phase, as shown in Fig. 16, indicated by the widening of the peak at 2theta = 45° (FWHM powder = 0.22 vs. printed = 0.31), matching the position of the α-FeSi peak. Prior studies on amorphous FINEMET material have indicated the evolution of the crystalline α-Fe phase followed by the Fe2B phase at higher temperatures. The consistently coexisting samples contain α-Fe (Si), Fe3Si, and Fe2B phases in the metal matrix. This observation aligns with those results, as gas-atomized precursor particles are likely to allow such evolution upon successive heat treatment.

The printed components, upon comparison, do not show any significant phase variation concerning the laser parameters, namely laser power and scan rate. However, a variation in the peak broadening has been recorded in the respective FWHM (Full Width at Half Maximum) of the most prominent peaks at 2theta = 46°, 67°, and 84°. Since all the patterns are recorded using the same X-ray diffractometer, the effect of instrument broadening may be canceled out. Quantifying the peak broadening and correlating it with the crystallite size using Scherrer's equation reveals a variation of nearly 76% in the solid components. Other processes, such as conventional sintering and melt-spun forms of these alloys, have been reported with a crystallite size of ~28 nm based on this calculation. Another report on SLM-processed FINEMET alloy also

indicated a large crystallite size variation, ranging from 10 to 24 nm, which is in line with our observation [35]. The comparatively stable Fe2B phase is also present alongside the dominant α-Fe (Si) peaks. The analysis of the Fe2B peaks relies on the XRD database, in which two of the Fe2B peaks are hidden in the background. Dr. Dos Santos's group has reported the DSC characterization of crystalline phase evolution of Fe-Si-B ribbons concerning changes in thermal conditions. The crystalline transition from the amorphous phases involves two to three steps. α-Fe (Si) and Fe3B form simultaneously at the beginning of crystallization, and the Fe3Si phase emerges as well as the transition from metastable Fe3B to Fe2B occurs in the first stage [12]. However, due to the closely spaced characteristic peaks of the α-FeSi, Fe2B, and Fe3Si phases in this alloy (Fig. 17), the respective phase fraction may also affect the peak broadening, which is the main input parameter in the Scherrer's equation, making the peak broadening data less conclusive, specifically for the crystallite size estimation. Although it is clear that the phase fraction of the Fe2B phase is minimal, as indicated by the relative intensities of the peaks since only the two highest intensity peaks of this phase are observable. Thus, the development of complicated thermal gradients during the solidification process in SLM, especially at relatively high laser energy density (power divided by scanning speed), could potentially further degrade the amorphous phase in the metal matrix. This theory has been developed by Dr. Nam's research group, revealing that a higher percentage of amorphous content prefers the lower energy density condition, and crystallization and grain growth are more severe at high laser energy density conditions [36]. This shows that the α-FeSi (matrix phase) and Fe3Si (segregated crystallite) are the dominant phases present, and their respective amounts may vary depending on the laser processing parameters.

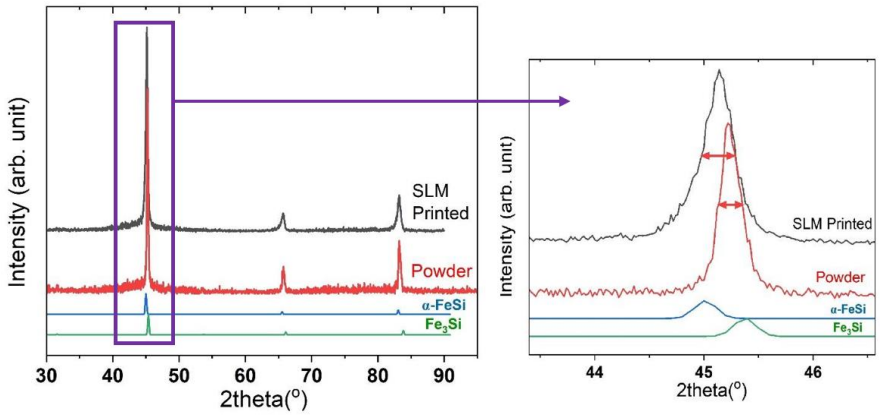

Figure 16: XRD pattern comparison between the FINEMET powder and the SLM printed component showing variation in the respective phase distribution.

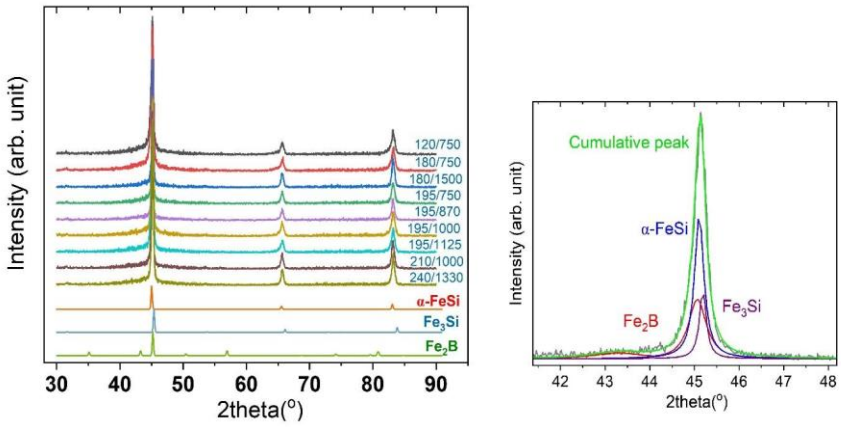

Figure 17: XRD pattern comparison of the SLM printed components at various laser parameters and the deconvoluted peaks of phases identified (α-FeSi, Fe3Si, Fe2B) as shown in the zoomed-in format for the peak close to 2theta 45.

The standard α-FeSi, Fe3Si, and Fe2B crystallize in a body-centered cubic, Heusler (cubic), and tetragonal crystal lattice, as obtained from the standard ICSD collection codes 103624, 658523, and 603829, respectively, and are shown for reference in Fig. 17. Based on the relative intensity observations, it can be asserted that α-FeSi and Fe3Si constitute the majority phase

fraction in the printed samples, as expected given the precursor composition. In general, all nine samples with different processing parameters exhibit a similar XRD peak pattern. However, localized variations in the 2-theta degree of low-intensity peaks can be observed. Calculating the crystallite size is more important than solely focusing on XRD pattern alignment, as it is closely related to the ferromagnetism of soft magnetic materials. With the observed peak broadening in these nine samples, SEM and EBSD analyses can be conducted to further address microstructural and crystalline orientation details.

3.4 SEM of grain structure and crystalline phases

SEM characterization, along with EDS and EBSD detectors, provides an in-depth understanding of the metal matrix features, component distribution, grain morphology, and crystalline texture (preferred/easy axis of grains) on the cross-section. At low magnification, the overall melt pool morphology is visible, with a high aspect ratio of micro-cracks propagating through the cross-section along the BD. No significant lack of fusion pores and keyholes are visible in the area of interest. Due to the 67° angular rotation during the multi-layer scanning process, melt pool morphology shapes share the same pattern and size, but the remelting/overlaps and reheating zones between adjacent melt pools are not identical. Individual melt pools present various types of metal matrix structures. Since the Finemet alloy typically has an amorphous structure initially, crystallization of α-Fe (Si) and Fe2B phases occurs, embedded in the amorphous matrix, followed by the transition from disordered α-Fe (Si) to ordered Fe3Si phase under preferred thermal conditions [37].

The cross-section of SLM-fabricated samples can be divided into four distinctive regions at the intersection of two melt pools in adjacent layers. Melt pool (MP) illustrates the area where, during subsequent layer scanning, a portion of the melt pool from the previous layer would be remelted at the top of the solidified layer and merge into the new melt pool in subsequent layers. Melt pool boundary (MPB) demonstrates the edge of an individual melt pool and illustrates the melt pool morphology with specific microstructural features. The heat-affected zone (HAZ), as explained in the previous section, has a significant impact on the microstructure by conducting heat from subsequent layers to solidified layers. Sufficient energy offers the thermal environment for phase evolution and solute segregation corresponding to the G/R ratio and undercooling. The melt pool top describes the area in the middle at the top of melt pools. In this area, the solidified alloy does not experience any severe thermal influences on its microstructure during the process of multi-layer deposition.

Fig. 18a provides a broad view of melt pool morphology at low magnification. Overlapped melt pools are aligned along the BD with no clear lack of fusion defects detected. Melt pool boundaries clearly separate each individual melt pool from each other. A keyhole-trapped air bubble can be observed with a spherical shape. Heterogeneously microcrack propagation on the cross-section typically penetrates through a few layers. In Fig. 18b, various solidification microstructures of metallic phases are presented with distinctive features at localized positions at the intersection of melt pools. Dendritic structures of metallic phases predominantly form at the middle top of the melt pool. Equiaxial grain structures are found to be homogeneously distributed in the melt pool, regardless of the spatial location. Spherical dendrites, segregated from the solidifying matrix at a high solidification rate at the melt pool boundary, exhibit a strong localization feature. The HAZ can be identified as two regions, including the transition regime and

the heat conduction regime. The transition regime suggests the gradual replacement of metallic phases from spherical dendrites to equiaxed dendritic structures. The heat conduction regime suggests that a portion of the previous solidified layers experiences the thermal effects from subsequent layers, resulting in grain coarsening over time.

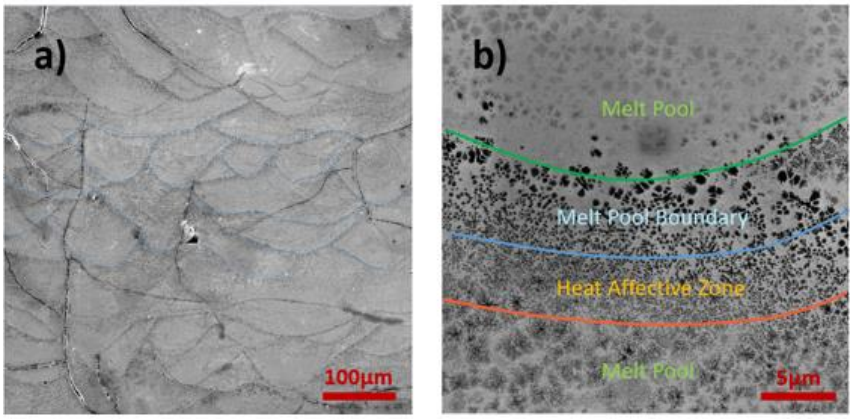

Figure 18: a) SEM image of multi-layer melt pool structure at low magnitude, b) interface of melt pools can be divided into three different zones including melt pool zone, melt pool boundary and heat affective zone.

Figs. 19a and 19b collaborate to present one of the representative single melt pool structures at high magnification, revealing various solidification structures. Due to the heterogeneous thermal environment induced by the multi-layer deposition of the SLM machine, the dendritic structure of the disordered α-Fe (Si) bcc phase predominates at the top of the MP area and in the HAZ due to variations in undercooling at different positions in the melt pool. The morphology of the solidified metallic phase, driven by the G/R ratio, suggests that an equiaxial grain structure prefers to form at relatively low undercooling corresponding to a high cooling rate.

Within one melt pool, the laser spot interacts with the central top of the powder and then gradually melts the edge of the melt pool, generating maximum energy and heat with a limited solidification rate due to the accumulated heat. Additionally, the melted material and central top of the melt pool efficiently transfer heat through thermal convection and radiation. Thus, a finer and equiaxial grain structure prefers to form at low undercooling, as described. Alternatively, the solidification process at the MPB experiences the least amount of heat (low temperature), resulting in a large undercooling compared to the middle top region of the melt pool. A superior cooling rate exacerbates the solute segregation of boride in the form of spherical dendrites at the MPB. Solute segregation usually occurs when the solidification of the material is faster than the diffusion of solute atoms into the solidifying material. However, the solidification mechanism is not solely dependent on the G/R and undercooling as contributing factors. Doped Nb atoms play an important role in impeding grain growth and facilitating the nucleation of equiaxial grains around the Cu atoms as nucleation sites. The homogeneous growth of the equiaxial grain structure of the disordered α-Fe (Si) phase in Fig. 19c occurs due to the large content of α-Fe (Si) in the metal matrix. Equiaxial grains continuously expand and consume the original amorphous matrix given enough time and temperature. This characterizes the uniform size of the equiaxial grain structure with embedded arbitrary shapes of the amorphous zone (grey area) at the bottom of the melt pool. The complete disappearance of the amorphous feature at the HAZ and top of the melt pool provides evidence of a sufficient cooling rate.

Additionally, the microstructure shows a partial phase transition from equiaxial grains to dendritic structures at the MP area, as shown in Fig. 19e. The well-established constitution of dendritic ordered Fe3Si phase is shown, with size distributions of each dendrite varying from hundreds of nanometers to 2 micrometers. Comparing this to the abundance of dendritic structures

at the HAZ, the trend of ordered-disordered phase transition starting from the top of the melt pool towards the bottom can be observed. At the melt pool boundary, the agglomeration of segregated spherical dendrites can be observed, with sizes ranging from 150 nm to 0.5 µm. To identify the composition of the metallic phase of such dendritic structures shown in Fig. 19f, the verification of the chemical composition of the dendritic structure was performed by EDS mapping and point scanning. Although the EDS detector does not provide promising results to reveal the actual composition from element to element in metal alloys, it contributes to our understanding of the overall composition and distribution within the dendritic structures.

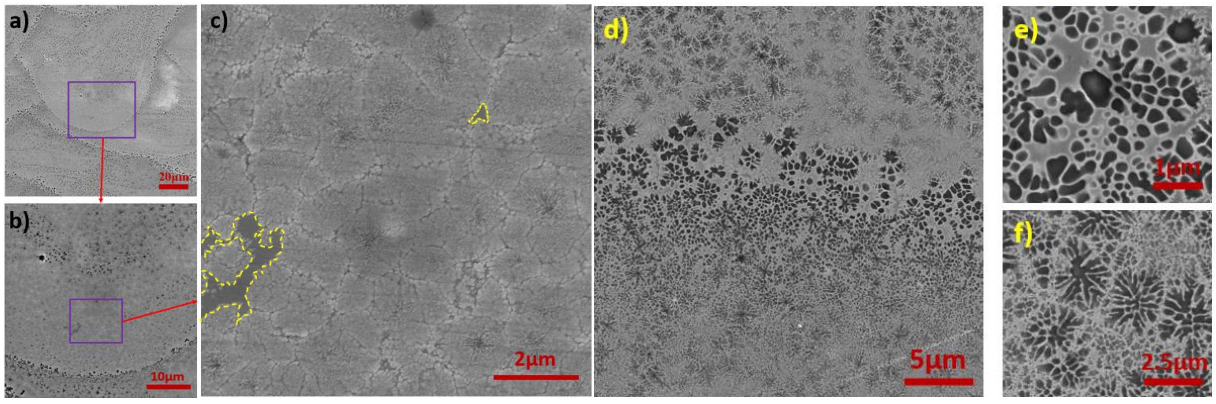

Figure 19: a), b) and c) are representing the melt pool zone with co-existing of distinctive equiaxial grains, dendrites and suspected amorphous phase under SEM of sample 195W-1.125m/s; d) shows the combination of spherical dendrites and equiaxed dendrites near the melt pool boundary, e) high magnitude of SEM image elucidates the spherical dendrites, f) illustrates equiaxed dendrites of sample 195W-1m/s.

Analysis can be derived from the results of comparing the mapping and point EDS analyses on individual elements, such as Boron content in the metal matrix. Fig. 20a shows the EDS mapping at the intersection of melt pools. The distinctive morphological features of metallic phases are visible in the combined elements image. The identical features of spherical dendrites can also be observed with the attached EDS detector. However, due to the relatively low atomic energy level of Boron atoms in the matrix, the signal from Boron is negligible when captured with other signals from elements with higher atomic energy levels. Thus, numerical results from the spectrum typically contain lower atomic percentages (< 1%) of Boron due to the technique's limitations in detecting Boron content. Therefore, the point EDS analysis in Fig. 20b, performed at a localized area with an atomic percentage spectrum containing more than 10% Boron, provides sufficient evidence for the presence of Boron-rich regions at the spot of interest.

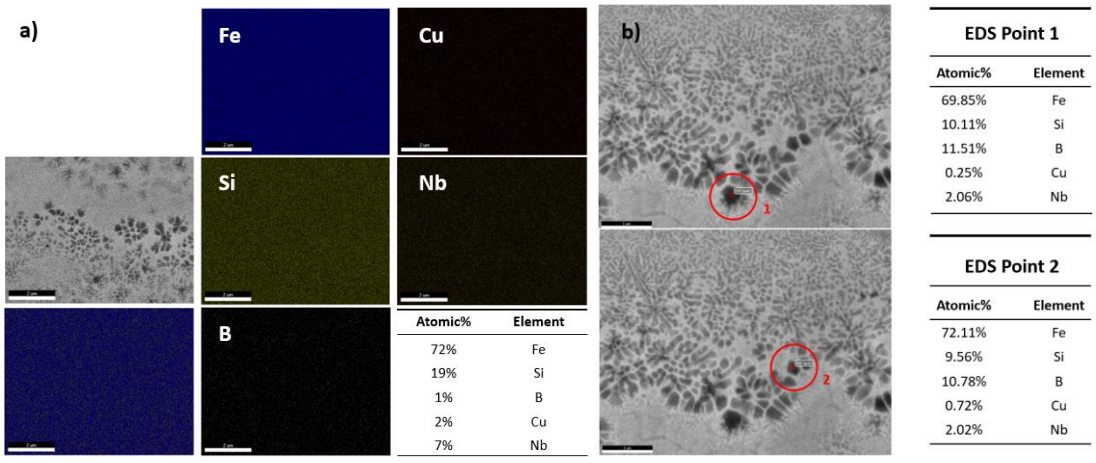

Atomic%	Element
72%	Fe
19%	Si
1%	B
2%	Cu
7%	Nb

EDS Point 1

Atomic%	Element
69.85%	Fe
10.11%	Si
11.51%	B
0.25%	Cu
2.06%	Nb

EDS Point 2

Atomic%	Element
72.11%	Fe
9.56%	Si
10.78%	B
0.72%	Cu
2.02%	Nb

Figure 20: a) EDS Mapping reveals the distribution of various elements from as-printed sample, b) Point EDS shows the localized boron rich content within the spherical dendrites of sample 195W-1m/s.

3.5 EBSD analysis of grain size distribution and crystalline texture

The EBSD mapping of an intersection area of multiple melt pools is shown in Fig. 21a. The inverse pole figure (IPF) illustrates the grain structure of the selected area with colored crystalline orientations along the BD. Significantly fine equiaxed grains dominantly spread out in the cross-section of the as-printed sample, regardless of the spatial position. Grain size distribution ranges from hundreds of nanometers to 2 μm, as revealed by the EBSD detector. Fig. 21b shows the grain boundary distribution on the cross-section, where blue traces represent high-angle grain boundaries, which are a key factor in characterizing grain structures, while green and red traces represent low-angle grain boundaries. The presence of low-angle boundaries could be the result of dislocation and defect formation during the solidification process, and the second theory suggests that the EBSD detector has the possibility of identifying the conjunction of finer grains (nano-scaled) as one coarser grain. The pole figure of the cross-section is shown in Fig. 21c, which describes the potential preferred crystallographic orientations of <001>, <111>, and <110> with respect to the axis direction of the as-printed samples. The colored spectrum bar refers to the amplitude of texture characterized from the pole figures. As a result, a homogeneous orientation of crystalline growth can be observed for the as-printed sample, with no potential crystallographic texture analyzed based on the IPF and pole figures. Fig. 21d illustrates further characterization of grain size distribution with respect to the localization at the cross-section. Grains highlighted within this area present grain sizes less than 1 μm. Due to the sophisticated solidification process with three metal phases embedded in the amorphous matrix, the EBSD mapping shows all metal phases with the same solidification morphology, making it difficult to specify the correlation. However, nano-scale grains are predominantly captured at the melt pool boundary, and based on the SEM/EDS characterization, the melt pool boundary is the boride-rich area. Thus, the average

grain size of boride at the melt pool boundary is significantly smaller than the grains within the melt pool. The grain size variation from the melt pool boundary to the center of the melt pool is due to the thermal history of the localization of the melt pool. The middle top of the melt pool experiences heat conducted from subsequent layers, leading to grain coarsening. Unfortunately, it is not possible to further visualize and analyze the grain size distribution with respect to morphological differences between the α-Fe (Si) and Fe3Si phases.

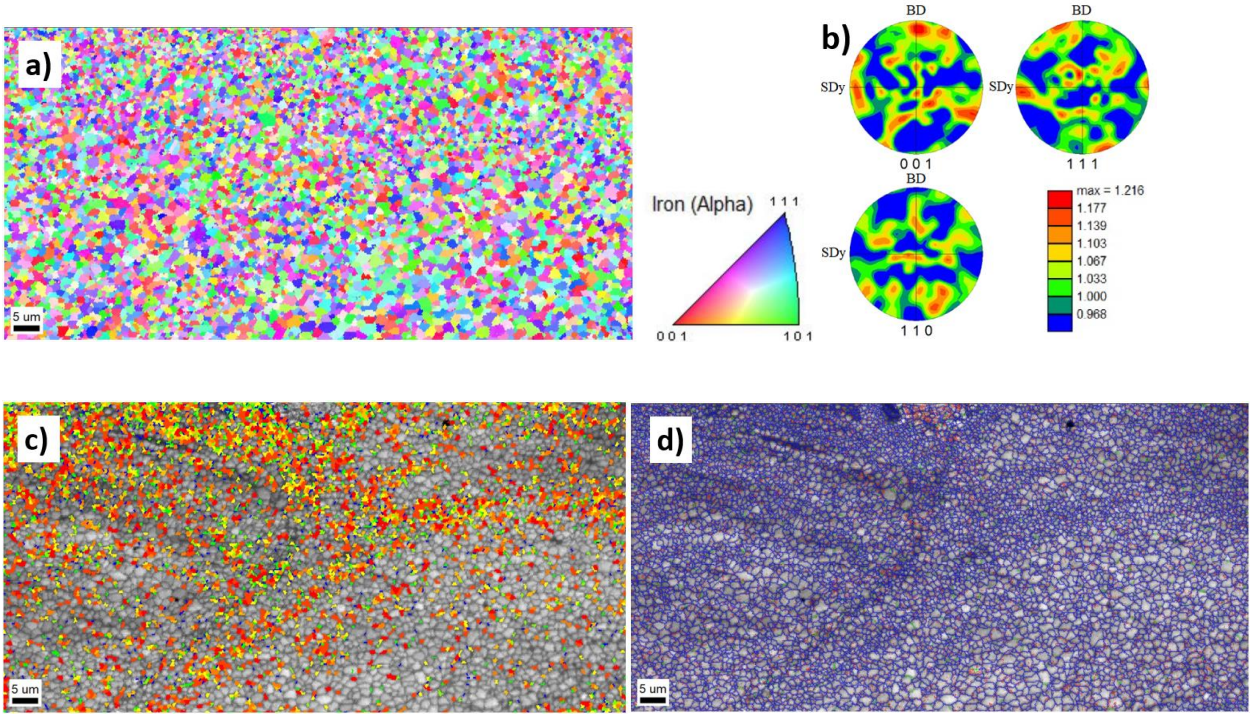

Figure 21: EBSD characterization to investigate the grain size distribution and potential texture; a) inverse pole figure shows grain structures and crystalline orientation, b) pole figure illustrates the potential texture within the area, c) highlighted grains possess grain size less than 1 µm, d) grain boundary distribution, various angle of misorientation at the grain boundary elucidated by different color.

3.6 VSM magnetic property characterization

In terms of the amorphous precursor embedded with nanocrystalline ferrite and boride, high saturation magnetization (Ms) can be significantly promoted due to the nature of the amorphous matrix, resulting in low coercivity by eliminating magneto-crystalline anisotropy. Conversely, the formation of crystalline or nanocrystalline structures is known to increase coercivity. Therefore, the temperature profile of different samples corresponding to various laser energy density inputs (J/m2) has a substantial impact on solidification, subsequently affecting the crystalline features and defect formation. The magnetic properties, including Ms and coercivity (Hc), among the nine different samples are characterized and shown in Fig. 22a. The variation of Ms, ranging from 124 to 136 emu/g, is schematically shown in Fig. 22b. The sample fabricated at 180W-1 m/s exhibits the highest Ms, while the lowest Ms is characterized at 180W-0.75m/s. In general, all characterized samples exhibit nanocrystalline features based on the observation of Ms. Furthermore, the limited range of Ms variation suggests the inadequate presence of the amorphous matrix within the alloy. Fig. 22c illustrates the amplitude of the remaining magnetic field (2 times of Hc) at the starting point of magnetization, ranging from 5.74 Oe to 29.82 Oe. The highest coercivity is presented by 180W-0.75 m/s, while the lowest coercivity is exhibited by 190W-1m/s.

Coercivity is the intrinsic magnetic property of soft magnetic materials that essentially correlates with magnetocrystalline anisotropy and results in the remnant flux in the soft magnetic material after the magnetization process. The principle of promoting a nanocrystalline structure on an amorphous precursor is intended to increase Ms while keeping coercivity relatively low. However, the nature of the nanocrystalline structure introduces coercivity, which can be averaged out by exchange interaction only if the nanocrystalline size is below the threshold, which is approximately 20 nm. Therefore, the coercivity of traditionally fabricated ribbons is mainly

influenced by defect formation due to the more controllable microstructure achieved through annealing. In L-PBF additive manufacturing, the observed α-Fe (Si), Fe_3Si, and Fe_2B phases exhibit size variations from hundreds of nanometers to a few micrometers, which result from the integration of subsequent reheating and reduced cooling rates. In this case, the characterized coercivity is the result of both grain size distribution of metallic phases and the formation of defects. The trend of coercivity with respect to laser energy input and bulk-scale density is illustrated in Fig. 22d, where a proportional relationship can be found between increased coercivity and higher laser energy density input. No significant difference can be observed based on bulk density, which could be due to the lack of sufficient data sets.

Table 1

Magnetic properties of Finemet and Finemet like Fe-based soft magnetic materials with traditional and AM manufacturing.

Material	**Ms (emu/g)**	**H_c (Oe)**	**Phases**	**Reference**
$Fe_{73.5}Si_{13.5}B_9Nb_3Cu_1$ (at%)	105	1.2	α-Fe (Si), Fe_3Si, Fe_2B	[38]
Plasma Nitriding				
Annealed (440 °C)				
$Fe_{73.5}Si_{13.5}B_9Nb_3Cu_1$ (at%)	122 - 166		α-Fe (Si), Fe_3Si, Fe_2B	[39]
Spark Plasma Sintering				
$Fe_{73.5}Si_{13.5}B_9Nb_3Cu_1$ (at%)	124 - 134	10 - 27	α-Fe (Si), Fe_3Si, Fe_2B	[40]
Melt Spinning				
$Fe_{84}Si_1B_{11}Nb_3Cu_1$	165	3.43		[41]
Melt Spinning				
$Fe_{73.5}Si_{13.5}B_9Nb_3Cu_1$ (at%)	124 - 136	5.74 - 29.82	α-Fe (Si), Fe_3Si, Fe_2B	Own Work
SLM				

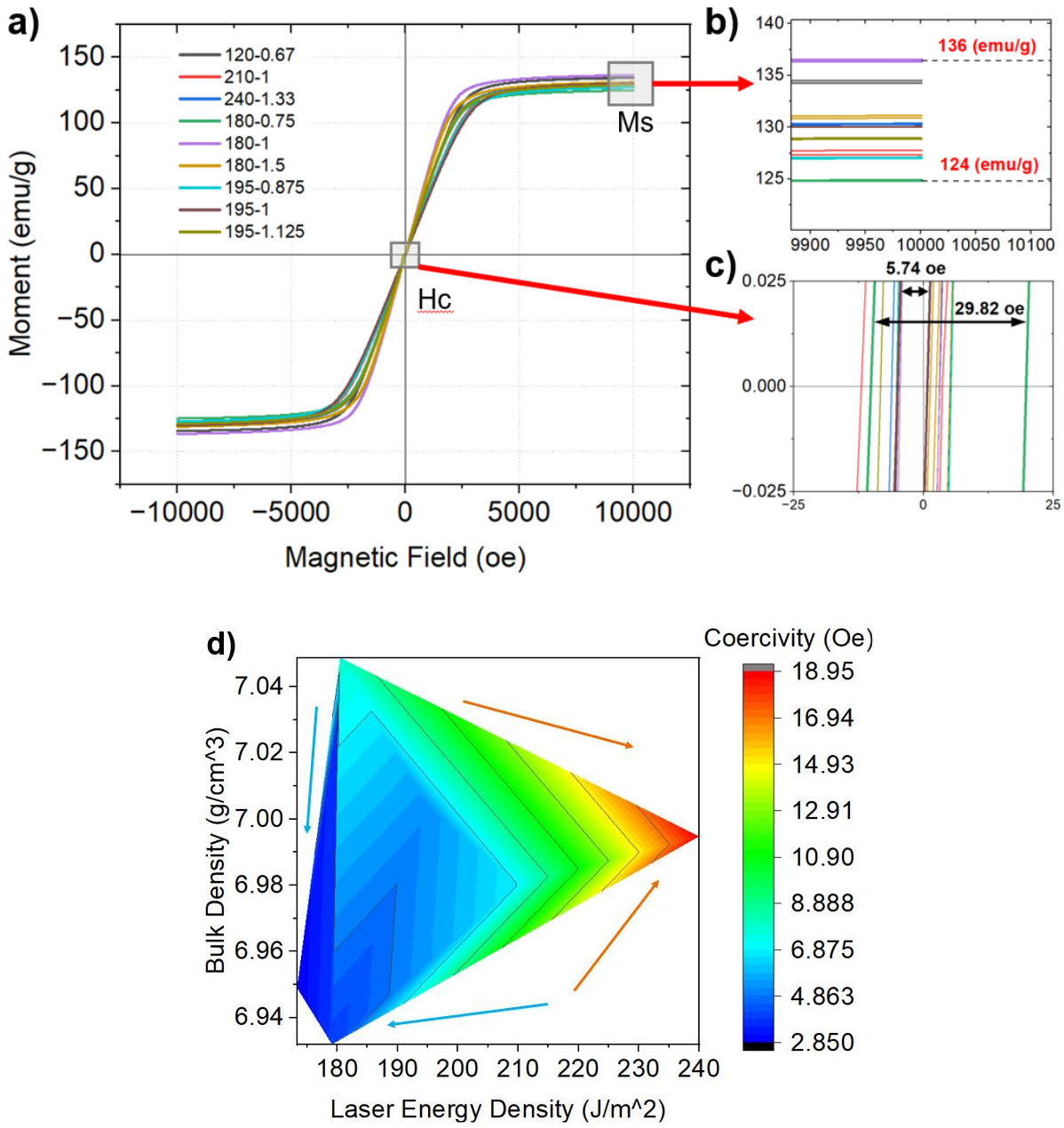

Figure 22: a) VSM characterized hysteresis loop of samples with various processing parameters, b) saturation magnetization variation, c) coercivity measurement at the origin, d) counter plot reveals the coercivity as a function of bulk-density and laser energy density input.

4. Conclusion and future works

4.1 Conclusion

Numerous advantages can be derived from L-PBF additive manufacturing technologies, primarily through the facilitation of intricate geometries and substantial reductions in manufacturing costs, particularly in comparison to traditional machining methods. However, there exists an economic trade-off, as it involves considering the costs of both the material powder and the additive manufacturing machine itself. Traditional soft magnetic materials, including amorphous and nanocrystalline alloys, require stringent cooling rates and precisely controlled thermal environments to achieve finer microstructure scales. The paradigm shift from the conventional melt spinning technique to the L-PBF AM technique, driven by the functional capabilities of SLM, offers exceptionally high cooling rates through adjustable processing parameters, particularly laser power, scanning speed, and layer thickness. This transition leverages a combination of factors that collectively create optimal solidification conditions, leading to the development of nano-scale grain structures and anticipated magnetic properties. In the scope of this research, the focus is on ensuring the printed quality and functional characteristics of SLM-fabricated components. Optical microscopy serves as a tool to identify macroscopic defects and melt pool morphologies, while Archimedes' density measurement aids in refining processing parameters. Moreover, XRD analysis elucidates the crystalline phases, and comprehensive microstructural insights are derived from SEM supplemented by EDS and EBSD detectors, offering a comprehensive examination of the metal matrix. In addition, magnetic properties are assessed using VSM which elucidates hysteresis loop characteristics, including saturation magnetization and coercivity, corresponding to different processing parameters and bulk densities.

The main contributions throughout this research study are listed below.

(1) Reveals the possibility of fabricating Finemet nanocrystalline material by SLM with optimized processing parameters and turn out to provide decent bulk-density. Relatively high saturation magnetization and low coercivity from sample 180W-1m/s also brings almost 95% of density.

(2) Characterized homogeneous distribution of α-Fe (Si) and ordered Fe_3Si phases mostly at the middle top of the melt pool along the BD. Segregated boron rich area at the melt pool boundary shows distinguish spherical dendrites feature suggests the large amount of undercooling at the melt pool boundary. Transition regime at the HAZ illustrates metallic phase transition from spherical dendrites (Fe_2B) to equiaxed dendrites (Fe_3Si).

(3) The consummation of 'amorphous' matrix by crystalline phases was evidenced under SEM of observing fine nanocrystals agglomerating and forming larger ones in grey area (no visible crystalline structure).

(4) Regardless of the bulk-density, higher laser energy input during the SLM fabrication process introduce high amplitude of coercivity among characterized samples. Thus, reasonable susception of higher energy density of providing suitable thermal environment and subsequent reheating promote the crystalline growth.

The cross-sectional analysis of melt pool size and morphologies reveals consistent features within the same layer, while distorted melt pool structures become evident in subsequent layers due to angular rotation. Observations demonstrate the presence of four distinct regions with arbitrary shapes spanning from the top to the bottom of the melt pool.

XRD analysis presented three distinct diffraction peak patterns, each pattern individually representing one of the metallic phases: α-Fe (Si), Fe_3Si, and Fe_2B. It's noteworthy that the Fe_2B

phase might be obscured due to its lower intensity amid the dominant α-Fe (Si) peaks. Within the confines of a single melt pool, several regions experiencing varying thermal environments were highlighted, providing a concise understanding of metallic phase formation in terms of the solidification mechanism.

Microstructures of grain sizes ranging from hundreds of nanometers to a few micrometers were homogeneously captured within the melt pool. Notably, the Boron-rich melt pool boundary exhibited spherical dendritic structures. EDS characterization of the melt pool boundary revealed a substantial Boron content, suggesting solute segregation at the boundary. EBSD identified grain boundaries that correlated well with the SEM analysis of grain size distribution. Smaller grains, typically less than 1 micron, were more prevalent along the melt pool boundary. Additionally, EBSD detected low-angle grain boundary misorientations within larger grains, hinting at potential agglomeration of nano-sized grains attributed to the finite resolution of the detector.

Furthermore, grey areas beneath the EBSD detector exhibited identical grain sizes as the time step, indicating the presence of an amorphous matrix. EBSD was unable to discern this amorphous phase, instead depicting fine and randomly oriented nano-grains. On the cross-section of the characterized sample, no discernible texture was detected, as indicated by the low intensity of the IPF spectrum. Across the entire cross-section, equiaxed α-Fe (Si) grains, equiaxed dendrites of Fe3Si, and spherical dendrites of Fe_2B phases were observed without any discernible preferred orientation. This observation suggests that the scanning strategies employed during the printing process, including double scanning and 67° angular rotation, effectively minimized crystalline orientation features, thereby mitigating magnetocrystalline anisotropy and reducing core loss.

4.2 Future works

The additive manufacturing of Finemet nanocrystalline material presents limitations across different dimensions. Core loss, dependent on hysteresis and eddy current losses during application, poses challenges when introducing insulation layers between Finemet alloy layers. This necessitates careful design to eliminate eddy currents, which could complicate powder arrangement. Moreover, the high Si content in Finemet alloys introduces microcracks and intermetallic disconnections, potentially impacting domain wall motion and coercivity.

Uncertainties arise during the printing process, including powder spattering and varying cooling rates due to thermal gradients across the substrate. In this study, multiple samples with diverse processing parameters were fabricated at different positions on the substrate, yielding significantly varied bulk densities. Further parameter optimization is essential to accurately delineate these boundaries and confirm repeatability. The focus of this research was to demonstrate the feasibility of observing nano-sized grains through rapid cooling driven by power and scanning speed, while maintaining decent bulk density. Optimal magnetic performance showcased coercivity below 10 Oe and a high saturation magnetization of 136 emu/g. The distribution of coarser grain sizes, spanning from hundreds of nanometers to a few micrometers, compared to traditional manufacturing techniques, requires improvement to mitigate reheating effects during the printing process.

For a comprehensive understanding of the printed samples, future work should encompass detailed characterization methods as TEM and Kerr microscopy. These techniques would shed light on nano-crystal orientation and magnetic domain structures, providing intrinsic insights into the as-printed samples.

References

[1] "https://www.electricalvolt.com/2019/11/hysteresis-loop/."

[2] M. E. McHenry, M. A. Willard, and D. E. Laughlin, "Amorphous and nanocrystalline materials for applications as soft magnets," *Prog Mater Sci*, vol. 44, no. 4, pp. 291–433, Oct. 1999, doi: 10.1016/S0079-6425(99)00002-X.

[3] K. Han, M. Saito, J. Xia, I. Ohnuma, and R. Kainuma, "Experimental determination of phase diagram involving silicides in the Fe-Si binary system," *J Alloys Compd*, vol. 919, p. 165810, Oct. 2022, doi: 10.1016/j.jallcom.2022.165810.

[4] D. S. Dos Santos and D. R. Dos Santos, "Crystallization kinetics of Fe-B-Si metallic glasses." [Online]. Available: www.elsevier.com/locate/jnoncrysol

[5] B. López-Walle, E. López-Cuellar, E. Reyes-Melo, O. Lomas-González, and W. de Castro, "A Smart Polymer Composite Based on a NiTi Ribbon and a Magnetic Hybrid Material for Actuators with Multiphysic Transduction," *Actuators*, vol. 4, no. 4, pp. 301–313, Dec. 2015, doi: 10.3390/act4040301.

[6] "https://openadditive.com/#panda."

[7] Y. Lee, M. Nordin, S. S. Babu, and D. F. Farson, "Effect of Fluid Convection on Dendrite Arm Spacing in Laser Deposition," *Metallurgical and Materials Transactions B*, vol. 45, no. 4, pp. 1520–1529, Aug. 2014, doi: 10.1007/s11663-014-0054-7.

[8] J. Qin, P. Yang, W. Mao, and F. Ye, "Effect of texture and grain size on the magnetic flux density and core loss of cold-rolled high silicon steel sheets," *J Magn Magn Mater*, vol. 393, pp. 537–543, Nov. 2015, doi: 10.1016/j.jmmm.2015.06.032.

[9] SoShin Chikazumi, "Physics of ferromagnetism".

[10] H. Kronmüller and S. Parkin, Eds., *Handbook of Magnetism and Advanced Magnetic Materials*. Wiley, 2007. doi: 10.1002/9780470022184.

[11] R. Hasegawa, *Glassy Metals: Magnetic, Chemical, and Structural Properties*. CRC Press, 2018. doi: 10.1201/9781351072267.

[12] G. Herzer, "Modern soft magnets: Amorphous and nanocrystalline materials," *Acta Mater*, vol. 61, no. 3, pp. 718–734, Feb. 2013, doi: 10.1016/j.actamat.2012.10.040.

[13] T. Gheiratmand and H. R. M. Hosseini, "Finemet nanocrystalline soft magnetic alloy: Investigation of glass forming ability, crystallization mechanism, production techniques, magnetic softness and the effect of replacing the main constituents by other elements," *J Magn Magn Mater*, vol. 408, pp. 177–192, Jun. 2016, doi: 10.1016/j.jmmm.2016.02.057.

[14] R. Parsons, B. Zang, K. Onodera, H. Kishimoto, A. Kato, and K. Suzuki, “Soft magnetic properties of rapidly-annealed nanocrystalline Fe-Nb-B-(Cu) alloys,” *J Alloys Compd*, vol. 723, pp. 408–417, Nov. 2017, doi: 10.1016/j.jallcom.2017.06.208.

[15] Y. Yoshizawa, S. Oguma, and K. Yamauchi, “New Fe-based soft magnetic alloys composed of ultrafine grain structure,” *J Appl Phys*, vol. 64, no. 10, pp. 6044–6046, Nov. 1988, doi: 10.1063/1.342149.

[16] K. Hono, K. Hiraga, Q. Wang, A. Inoue, and T. Sakurai, “The microstructure evolution of a Fe73.5Si13.5B9Nb3Cu1 nanocrystalline soft magnetic material,” *Acta Metallurgica et Materialia*, vol. 40, no. 9, pp. 2137–2147, Sep. 1992, doi: 10.1016/0956-7151(92)90131-W.

[17] V. R. V. Ramanan and G. E. Fish, “Crystallization kinetics in Fe−B−Si metallic glasses,” *J Appl Phys*, vol. 53, no. 3, pp. 2273–2275, Mar. 1982, doi: 10.1063/1.330797.

[18] S. Ozawa, T. Saito, and T. Motegi, “Effects of cooling rate on microstructures and magnetic properties of Nd–Fe–B alloys,” *J Alloys Compd*, vol. 363, no. 1–2, pp. 268–275, Jan. 2004, doi: 10.1016/S0925-8388(03)00461-4.

[19] M. G. Ozden and N. A. Morley, “Laser Additive Manufacturing of Fe-Based Magnetic Amorphous Alloys,” *Magnetochemistry*, vol. 7, no. 2, p. 20, Jan. 2021, doi: 10.3390/magnetochemistry7020020.

[20] A. Krings, M. Cossale, A. Tenconi, J. Soulard, A. Cavagnino, and A. Boglietti, “Magnetic Materials Used in Electrical Machines: A Comparison and Selection Guide for Early Machine Design,” *IEEE Industry Applications Magazine*, vol. 23, no. 6, pp. 21–28, Nov. 2017, doi: 10.1109/MIAS.2016.2600721.

[21] H. Y. Jung *et al.*, “Fabrication of Fe-based bulk metallic glass by selective laser melting: A parameter study,” *Mater Des*, vol. 86, pp. 703–708, Dec. 2015, doi: 10.1016/j.matdes.2015.07.145.

[22] M. Garibaldi, I. Ashcroft, M. Simonelli, and R. Hague, “Metallurgy of high-silicon steel parts produced using Selective Laser Melting,” *Acta Mater*, vol. 110, pp. 207–216, May 2016, doi: 10.1016/j.actamat.2016.03.037.

[23] Y. Shen, Y. Li, and H.-L. Tsai, “Evolution of crystalline phase during laser processing of Zr-based metallic glass,” *J Non Cryst Solids*, vol. 481, pp. 299–305, Feb. 2018, doi: 10.1016/j.jnoncrysol.2017.11.001.

[24] B. Müller and C. Fraunhofer IWU, *Fraunhofer Direct Digital Manufacturing Conference DDMC 2016. Conference Proceedings, March 2016, Berlin, Germany.*

[25] D. Ouyang, W. Xing, N. Li, Y. Li, and L. Liu, “Structural evolutions in 3D-printed Fe-based metallic glass fabricated by selective laser melting,” *Addit Manuf*, vol. 23, pp. 246–252, Oct. 2018, doi: 10.1016/j.addma.2018.08.020.

[26] Y. Huang *et al.*, “Keyhole fluctuation and pore formation mechanisms during laser powder bed fusion additive manufacturing,” *Nat Commun*, vol. 13, no. 1, p. 1170, Mar. 2022, doi: 10.1038/s41467-022-28694-x.

[27] T. M. Wischeropp, C. Emmelmann, M. Brandt, and A. Pateras, “Measurement of actual powder layer height and packing density in a single layer in selective laser melting,” *Addit Manuf*, vol. 28, pp. 176–183, Aug. 2019, doi: 10.1016/j.addma.2019.04.019.

[28] M. J. Matthews, G. Guss, S. A. Khairallah, A. M. Rubenchik, P. J. Depond, and W. E. King, “Denudation of metal powder layers in laser powder bed fusion processes,” *Acta Mater*, vol. 114, pp. 33–42, Aug. 2016, doi: 10.1016/j.actamat.2016.05.017.

[29] J. H. Robinson, I. R. T. Ashton, E. Jones, P. Fox, and C. Sutcliffe, “The effect of hatch angle rotation on parts manufactured using selective laser melting,” *Rapid Prototyp J*, vol. 25, no. 2, pp. 289–298, Mar. 2019, doi: 10.1108/RPJ-06-2017-0111.

[30] M. Dimter, R. Mayer, L. Hummeler, R. Salzberger, J. Kotila, and T. Syvanen, “United States US 20080241392A1 (12) Patent Application Publication (10) Pub.”

[31] T. Cullom *et al.*, “Frequency domain measurements of melt pool recoil force using modal analysis,” *Sci Rep*, vol. 11, no. 1, p. 10959, May 2021, doi: 10.1038/s41598-021-90423-z.

[32] M. Seiler, A. Patschger, and J. Bliedtner, “Investigations of welding instabilities and weld seam formation during laser microwelding of ultrathin metal sheets,” *J Laser Appl*, vol. 28, no. 2, May 2016, doi: 10.2351/1.4944446.

[33] T. R. Anthony and H. E. Cline, “Surface rippling induced by surface-tension gradients during laser surface melting and alloying,” *J Appl Phys*, vol. 48, no. 9, pp. 3888–3894, Sep. 1977, doi: 10.1063/1.324260.

[34] T. Gheiratmand, H. R. Madaah Hosseini, P. Davami, and C. Sarafidis, “Fabrication of FINEMET bulk alloy from amorphous powders by spark plasma sintering,” *Powder Technol*, vol. 289, pp. 163–168, Feb. 2016, doi: 10.1016/j.powtec.2015.11.060.

[35] T. Larimian, V. Chaudhary, M. U. F. Khan, R. V. Ramanujan, R. K. Gupta, and T. Borkar, “Spark plasma sintering of Fe–Si–B–Cu–Nb / Finemet based alloys,” *Intermetallics (Barking)*, vol. 129, p. 107035, Feb. 2021, doi: 10.1016/j.intermet.2020.107035.

[36] Y. G. Nam *et al.*, “Selective laser melting vitrification of amorphous soft magnetic alloys with help of double-scanning-induced compositional homogeneity,” *Mater Lett*, vol. 261, p. 127068, Feb. 2020, doi: 10.1016/j.matlet.2019.127068.

[37] Ł. Żrodowski *et al.*, “New approach to amorphization of alloys with low glass forming ability via selective laser melting,” *J Alloys Compd*, vol. 771, pp. 769–776, Jan. 2019, doi: 10.1016/j.jallcom.2018.08.075.

[38] H. A. Shivaee, H. R. M. Hosseini, E. M. Lotfabad, and S. Roostaie, “Study of nanocrystallization in FINEMET alloy by active screen plasma nitriding,” *J Alloys Compd*, vol. 491, no. 1–2, pp. 487–494, Feb. 2010, doi: 10.1016/j.jallcom.2009.10.240.

[39] T. Larimian, V. Chaudhary, M. U. F. Khan, R. V. Ramanujan, R. K. Gupta, and T. Borkar, “Spark plasma sintering of Fe–Si–B–Cu–Nb / Finemet based alloys,” *Intermetallics (Barking)*, vol. 129, p. 107035, Feb. 2021, doi: 10.1016/j.intermet.2020.107035.

[40] T. Gheiratmand, H. R. M. Hosseini, P. Davami, M. Gjoka, and M. Song, “The effect of mechanical milling on the soft magnetic properties of amorphous FINEMET alloy,” *J Magn Magn Mater*, vol. 381, pp. 322–327, May 2015, doi: 10.1016/j.jmmm.2015.01.016.

[41] J. Han, S. Kwon, S. Sohn, J. Schroers, and H. Choi-Yim, “Optimum Soft Magnetic Properties of the FeSiBNbCu Alloy Achieved by Heat Treatment and Tailoring B/Si Ratio,” *Metals (Basel)*, vol. 10, no. 10, p. 1297, Sep. 2020, doi: 10.3390/met10101297.